

## Journal Pre-proofs

A comparison of five surface mixed layer models with a year of observations in the North Atlantic

Gillian M. Damerell, Karen J. Heywood, Daley Calvert, Alan L. M. Grant, Michael J. Bell, Stephen E. Belcher

PII: S0079-6611(20)30055-0

DOI: <https://doi.org/10.1016/j.pocean.2020.102316>

Reference: PROOCE 102316

To appear in: *Progress in Oceanography*

Received Date: 2 May 2019

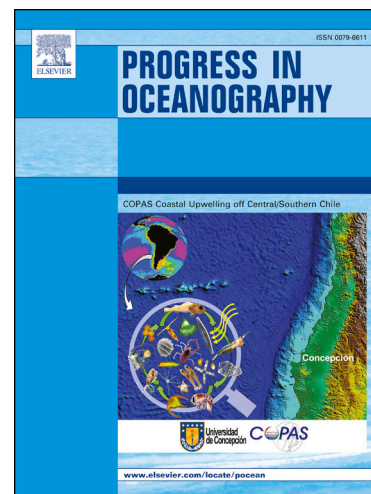
Revised Date: 12 December 2019

Accepted Date: 18 March 2020

Please cite this article as: Damerell, G.M., Heywood, K.J., Calvert, D., M. Grant, A.L., Bell, M.J., Belcher, S.E., A comparison of five surface mixed layer models with a year of observations in the North Atlantic, *Progress in Oceanography* (2020), doi: <https://doi.org/10.1016/j.pocean.2020.102316>

This is a PDF file of an article that has undergone enhancements after acceptance, such as the addition of a cover page and metadata, and formatting for readability, but it is not yet the definitive version of record. This version will undergo additional copyediting, typesetting and review before it is published in its final form, but we are providing this version to give early visibility of the article. Please note that, during the production process, errors may be discovered which could affect the content, and all legal disclaimers that apply to the journal pertain.

© 2020 Published by Elsevier Ltd.



# A comparison of five surface mixed layer models with a year of observations in the North Atlantic

Gillian M. Damerell<sup>a,\*</sup>, Karen J. Heywood<sup>a</sup>, Daley Calvert<sup>b</sup>, Alan L. M. Grant<sup>c</sup>, Michael J. Bell<sup>b</sup>, Stephen E. Belcher<sup>b</sup>

<sup>a</sup>*Centre for Ocean and Atmospheric Sciences, School of Environmental Science, University of East Anglia, Norwich, United Kingdom*

<sup>b</sup>*Met Office, Hadley Centre, FitzRoy Road, Exeter, Devon, United Kingdom*

<sup>c</sup>*Department of Meteorology, University of Reading, Reading, United Kingdom*

---

## Abstract

Five upper ocean mixed layer models driven by ERA-Interim surface forcing are compared with a year of hydrographic observations of the upper 1000 m, taken at the Porcupine Abyssal Plain observatory site using profiling gliders. All the models reproduce sea surface temperature (SST) fairly well, with annual mean warm biases of 0.11°C (PWP model), 0.24°C (GLS), 0.31°C (TKE), 0.91°C (KPP) and 0.36°C (OSMOSIS). The main exception is that the KPP model has summer SSTs which are higher than the observations by nearly 3°. Mixed layer salinity (MLS) is not reproduced well by the models and the biases are large enough to produce a non-trivial density bias in the Eastern North Atlantic Central Water which forms in this region in winter.

All the models develop mixed layers which are too deep in winter, with average winter mixed layer depth (MLD) biases between 160 and 228 m. The high variability in winter MLD is reproduced more successfully by model estimates of the depth of active mixing and/or boundary layer depth than by model MLD based on water column properties. After the spring restratification event, biases in MLD are small and do not appear to be related to the preceding winter biases.

There is a very clear relationship between MLD and local wind stress in all models and in the observations during spring and summer, with increased wind speeds leading to deepening mixed layers, but this relationship is not

---

\*Corresponding author

*Email address:* [g.damerell@uea.ac.uk](mailto:g.damerell@uea.ac.uk) (Gillian M. Damerell)

present during autumn and winter. We hypothesize that the deepening of the MLD in autumn is so strongly driven by the annual cycle in surface heat flux that the winds are less significant in the autumn. The surface heat flux drives a diurnal cycle in MLD and SST from March onwards, though this effect is much more significant in the models than in the observations.

We are unable to identify one model as definitely better than the others. The only clear differences between the models are KPP's inability to accurately reproduce summer SSTs, and the OSMOSIS model's more accurate reproduction of MLS.

*Keywords:* Ocean models, surface mixed layer, ocean gliders

---

## 1. Introduction

Climate models are important tools for understanding the climate and its response to various forcings (Flato et al., 2013). The surface mixed layer forms the boundary between the ocean and atmosphere, and regulates exchanges of heat, momentum and trace gases. The ability of the oceans to buffer atmospheric climate change by absorbing and then storing heat and radiatively important trace gases relies heavily upon the exchanges in the surface mixed layer (Belcher et al., 2012). Thus surface mixed layer parameterisations which accurately reproduce observed behaviour are a vital tool in developing climate models which can make reasonable predictions of the future response to anthropogenic activity.

Here we compare various 1D mixed layer models with observations (Damerell et al., 2016) of mixed layer properties taken over a full year in the Northeast Atlantic using profiling gliders, as part of the Ocean Surface Mixing, Ocean Submesoscale Interaction Study (OSMOSIS). Various properties are considered to compare the performance of the various models. First and foremost is the ability of the models to reproduce the observed sea surface temperature (SST), since this is of considerable importance for the exchange of heat with the atmosphere. Unlike at Ocean Station Papa (OSP), where Large et al. (1994) find that model/observation SST comparisons are only reliable from April to October because of the relative importance of net surface heat fluxes and advective fluxes at different times of year, Lazarevich et al. (2004) found that in the North Atlantic a modified form of the Price-Weller-Pinkel mixed layer model, using NCEP-derived surface forcing, accurately reproduced float-observed temperatures and meteorological-based SSTs to within

26 1°C for an entire year. Moreover, Damerell et al. (2016), using the same ob-  
27 servational dataset as used here, found that the mixed layer temperature is  
28 strongly correlated ( $r = 0.87$ ) with the cumulative net surface heat flux from  
29 ECMWF ERA-Interim reanalysis data (Dee et al., 2011). The main differ-  
30 ences were during the autumn, when cooler water from below is entrained  
31 into the mixed layer, and late summer, when the very shallow mixed layer  
32 depth (MLD) means that some of the absorption of solar radiation will occur  
33 below the mixed layer. These processes (entrainment of water from below  
34 and penetration of solar radiation) are represented in the models used here,  
35 so we expect the models to reproduce observed SST reasonably well for the  
36 whole year.

37 Mixed layer salinity (MLS) is discussed because of its impact on mixed  
38 layer density and MLD. (It was not practical to compare sea surface salinity  
39 as the nature of glider data collection means there are gaps in the surface  
40 salinity data after quality control.) Unlike SST, Damerell et al. (2016) find  
41 that the MLS of this dataset is not correlated with the surface freshwater  
42 fluxes from ERA-Interim though it is weakly correlated with the currents  
43 ( $r = 0.4$ ). They conclude that the changes in MLS must be influenced by  
44 advection into the area of water masses of different salinity and/or vertical  
45 mixing with waters of different salinity from the ocean interior, and while  
46 the latter may be reproduced in 1D models, the former is not. Hence we do  
47 not necessarily expect the MLS of the models to agree with the observations  
48 particularly well. We also compare the MLD, since this is an important factor  
49 in the development of the surface mixed layer and interaction with the ocean  
50 interior.

51 We discuss the coherence between observations and model output, and  
52 coherence with surface forcing. Note that we use potential temperature and  
53 practical salinity throughout, and all densities are potential density anomalies  
54 ( $\sigma_\theta$ ) relative to the surface and will be given without units.

55 Many other authors have compared 1D models to ocean observations,  
56 e.g., Large et al. (1994); Kantha and Clayson (1994); Burchard and Bold-  
57 ing (2001); Lazarevich et al. (2004); Acreman and Jeffery (2007); Pookkandy  
58 et al. (2016). However, this has generally been done using observations from  
59 moorings (such as OSP) where the limited vertical resolution will affect mea-  
60 surement of the MLD, or observations from floats which may have limited  
61 vertical and/or temporal resolution, or from ship CTDs which will not pro-  
62 vide long time series of profiles in one location. The profiling gliders used here  
63 provide profiles to 1000 m with a vertical resolution of 2 m, at approximately

64 2-hourly intervals for a whole year. Thus the observational data is partic-  
65 ularly well suited to comparisons with model output. The good temporal  
66 resolution also allows the application of wavelet coherence methods (section  
67 4) to this question.

68 Section 2 describes the observational data set with which the models will  
69 be compared. Section 3 summarizes the key features of each of the models  
70 and describes the model setup. The Price-Weller-Pinkel (PWP), K-Profile-  
71 Parameterisation (KPP), Generic Length Scale (GLS) and Turbulent Kinetic  
72 Energy (TKE) models are described extensively elsewhere (e.g., Price et al.,  
73 1986; Lazarevich and Stoermer, 2001; Large et al., 1994; Gaspar et al., 1990;  
74 Rodi, 1987) so we give only brief descriptions here. We include a more  
75 complete description of the recently developed OSMOSIS model. Section 4  
76 describes the wavelet analysis methods used to investigate the periodic be-  
77 haviour of the data and models. Section 5 presents the results and compares  
78 the model and observed behaviour, and section 6 contains the conclusions.

## 79 **2. Ocean glider observations of upper ocean hydrography**

80 The OSMOSIS project incorporated a year-long observational programme  
81 centred 41 km to the southeast of the Porcupine Abyssal Plain sustained  
82 observatory (PAP-SO; Lampitt et al., 2010a), with observations collected  
83 within a 15 km radius of  $48.7^\circ$  N,  $16.2^\circ$  W (figure 1). This location is con-  
84 sidered remote from the topographic complexities of the continental slope  
85 and the Mid-Atlantic Ridge (Hartman et al., 2012), and thus remote from  
86 places where strong internal tides might be generated. It is located in the  
87 inter-gyre region between the North Atlantic subpolar and subtropical gyres  
88 where the mean flow is relatively weak and eddy kinetic energy is moderate.  
89 The variability in physical properties is likely to be representative of large  
90 areas of the mid-latitude gyres.

91 As part of the OSMOSIS field campaign, profiling ocean gliders (Seaglid-  
92 ers) were deployed for periods varying between two and five months, between  
93 them covering an entire year from 4th September 2012 to 7th September 2013.  
94 The Seaglider dataset consists of 3785 profiles at approximately 2-hourly in-  
95 tervals of temperature and salinity to 1000 m, with a vertical resolution of 2  
96 m after gridding. Details of the sensors, data processing, quality control and  
97 calibration are given by Damerell et al. (2016). Temperature and salinity  
98 are considered accurate to  $0.01^\circ\text{C}$  and 0.01 respectively. The 15 km radius  
99 within which the observations were collected is comparable to the spacing

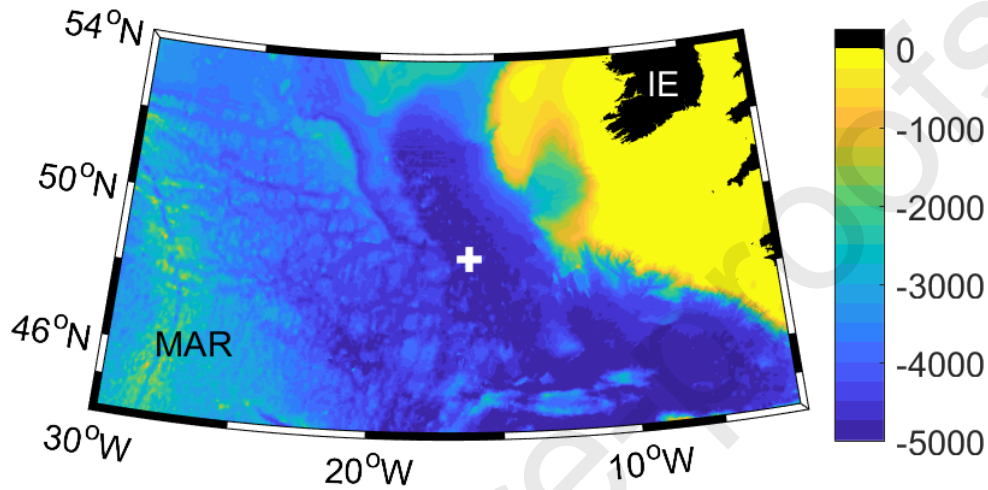


Figure 1: Bathymetry of the north-east Atlantic basin. The white cross marks the location of the OSMOSIS field campaign. MAR=mid-Atlantic Ridge. IE=Ireland.

100 between CTD locations of a typical ship-based hydrographic survey, and for  
 101 the purposes of this paper, we treat the data as if they had all been ob-  
 102 tained at the same location. There is an implicit linkage between spatial and  
 103 temporal variability in glider observations, and here we choose to treat it as  
 104 purely temporal variability.

105 The depth of the surface mixed layer is calculated using a threshold value  
 106 of temperature or density from a near-surface value at 5 m depth ( $\Delta T = 0.2^\circ\text{C}$   
 107 or  $\Delta\sigma_\theta = 0.03$ ), whichever is the shallower (de Boyer Montegut et al., 2004).  
 108 (MLD is calculated in the same manner for each model, see section 3.2.)  
 109 Thus, we aim to find the MLD even in cases where temperature and salinity  
 110 vary with depth in a density-compensating manner, as well as cases where  
 111 density varies with depth due to changes in salinity rather than temperature.  
 112 In 67% of the record the MLD is set by the density threshold, 19% by the  
 113 temperature threshold, and in 13% of the record the two thresholds give the  
 114 same MLD. There is no clear seasonal pattern in which threshold sets the  
 115 MLD. We chose 5 m as the reference depth because above that there are too



116 many gaps in the observational data due to the removal of salinity spikes  
 117 during quality control. Spiking in the near-surface is unfortunately common  
 118 in glider observations due to surface manoeuvres altering the flow of water  
 119 past the sensors, cooling or warming while at the surface and air bubbles and  
 120 particulates in/on sensors when leaving the surface. Note that this means  
 121 that MLDs shallower than 5 m cannot be identified.

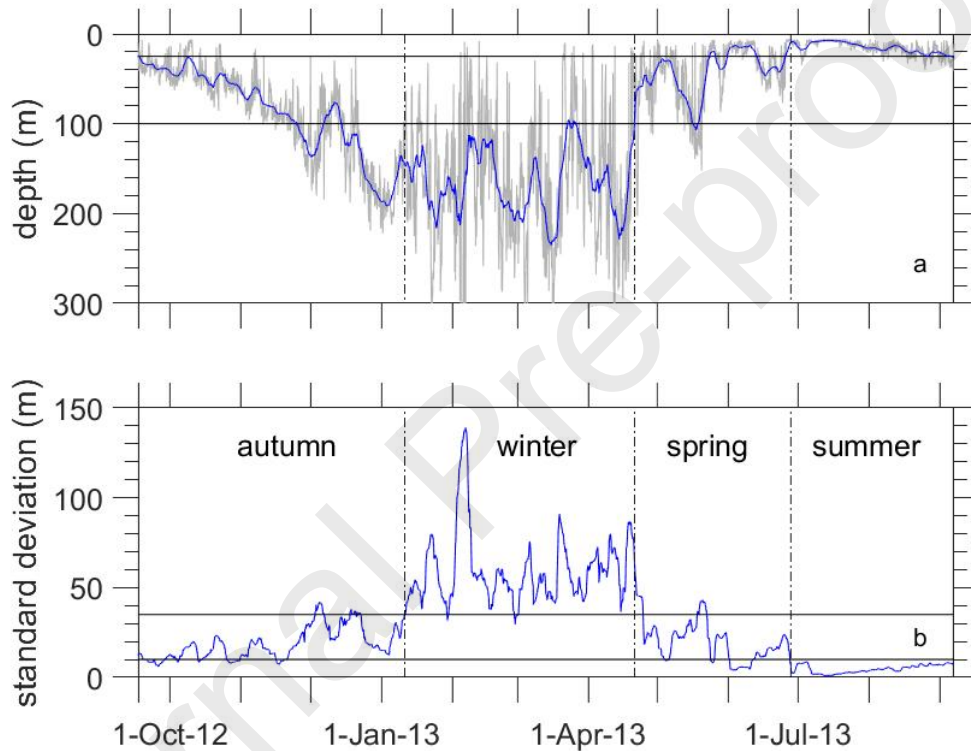


Figure 2: Definition of seasons as used in this paper. a) MLD calculated from the observations (gray), and running mean MLD (blue) calculated at each observation time over a 5-day window (i.e., with a window extending from 2.5 days before that observation time to 2.5 days after that observation time). Black horizontal lines are at 25 and 100 m. b) standard deviation of the observed MLD, calculated over a 5-day window as for the running mean MLD. This will be referred to as the running standard deviation of MLD. Black horizontal lines are at 10 and 35 m. Black vertical dotted lines on both panels show the dates which divide the year into seasons, as labeled on b).

122 We divide the year into four seasons based on the behaviour of the ob-  
 123 served MLD. The start of winter is deemed to be the day when the running

124 mean MLD, calculated over a 5 day window, is deeper than 100 m and the  
125 running standard deviation of MLD (calculated over the same 5 day window)  
126 is greater than 35 m (figure 2), and these criteria are fulfilled for a period  
127 of at least 5 days. In other words, winter is the period when the MLD is  
128 consistently deeper than 100m but is also quite variable due to the lack of  
129 a strong pycnocline within the upper water column (see below). The start  
130 of spring is deemed to be the day when the running mean MLD is shallower  
131 than 100 m and remains so for a period of at least a week, consistent with  
132 previous definitions used in this area (Lampitt et al., 2010b). Summer is  
133 deemed to be the period when the running mean MLD is shallower than 25  
134 m, and the running standard deviation of MLD is less than 10 m, i.e., the  
135 MLD is consistently shallow and shows low variability due to the presence of  
136 a strong pycnocline. Using these definitions, autumn is the period from the  
137 start of the time series on 24 September 2012 to 10 January 2013, winter is  
138 from 11 January to 20 April 2013, spring is from 21 April to 27 June 2013,  
139 and summer from 28 June to the end of the time series on 7 September 2013.

140 A strong, stable pycnocline forms in summer, then gradually erodes dur-  
141 ing the autumn, until during winter there is very weak stratification to consid-  
142 erable depth. Erickson and Thompson (2018), using the same dataset, found  
143 that this definition of MLD still retained credibility in winter as chlorophyll  
144 values become near-zero at approximately the same depth (their figure 5).  
145 However, the winter MLD is sensitive to the precise thresholds used and it  
146 may be more accurate to say that the base of the mixed layer is no longer  
147 very well defined because of the lack of a strong pycnocline within the upper  
148 water column.

### 149 **3. Models**

#### 150 *3.1. Model selection*

151 Although 1D models do not include full ocean physics and in particular  
152 the many lateral processes, this can allow for a cleaner inter-comparison of  
153 those processes which are included. The topics studied using 1D models vary  
154 widely. Some examples include: studies of the effect of new model processes  
155 (Chen et al., 1994) which is easier to do in a 1D model before integration  
156 into a full ocean model; studies of the effect of model resolution and tuning  
157 (Acreman and Jeffery, 2007); understanding physical processes varying from  
158 the role of local atmospheric forcing on mixed layer depth (Pookkandy et al.,  
159 2016), to tidally driven controls on the location of mixing fronts (Sheehan



160 et al., 2018), to glacial meltwater fractions in the polar oceans (Biddle et al.,  
161 2017); investigating net community production (Martz et al., 2008; Yang  
162 et al., 2017); understanding spring bloom dynamics (Sharples et al., 2006).

163 Models were chosen for this study to include commonly used examples  
164 of the range of approaches used to parameterise the surface mixed layer  
165 (see, for example, Burchard et al. (2008) for a discussion of the different  
166 approaches to this question). These models assume the turbulent mixing  
167 is dominated by vertical fluxes, and varying degrees of complexity are used  
168 to parameterise these fluxes. Perhaps the simplest approach is that of bulk  
169 boundary layers where ocean properties are assumed to be vertically uniform  
170 in the mixed layer. PWP (Price et al., 1986) is an example of this type: a  
171 computationally efficient bulk mixed layer model which has been used for  
172 many years to study ocean physics and biogeochemistry (e.g., Lazarevich  
173 et al., 2004; Frants et al., 2013; Viglione et al., 2018; Farahat and Abuelgasim,  
174 2019) due to its simplicity and ease of use (further details in section 3.3).

175 Another widely used approach is that of turbulent kinetic energy closure  
176 (TC), where the profiles of eddy diffusivity and viscosity are dependent on the  
177 local turbulent kinetic energy, which is prognostic (e.g., Mellor and Yamada,  
178 1982; Kantha and Clayson, 1994; Harcourt, 2015). The properties of the  
179 turbulent flow are modelled directly by solving the Reynolds budgets for the  
180 second-order moments. The GLS and TKE mixed layer models used here  
181 are examples of 'one-' and 'two-equation' TC schemes (see further details in  
182 section 3.5). GLS and TKE are implemented in the NEMO ocean modelling  
183 framework (Madec, 2008) which is widely used for climate modelling (see,  
184 for example, list of publications at <https://www.nemo-ocean.eu/>).

185 K-profile parameterisation models aim to fill the middle ground between  
186 bulk mixed layer models and TC schemes by allowing for vertical property  
187 variations in the mixed layer via a specified vertical shape function (Large  
188 et al., 1994). Vertical turbulent fluxes in the absence of vertical gradients of  
189 ocean properties are permitted through a non-local transport parameterisa-  
190 tion (Burchard et al., 2008; Van Roekel et al., 2018). The version used here  
191 is a single column of the Multi-Column K Profile Parameterisation mixed  
192 layer model (Hirons et al., 2015), which is used as a relatively computationally  
193 efficient alternative to a full ocean model in coupled atmosphere-ocean  
194 climate simulations and process studies (e.g., Lee and Klingaman, 2018; Hi-  
195 rons et al., 2018) (further details in section 3.4). Modifications to the KPP  
196 scheme to represent Langmuir turbulence (which arises through the interac-  
197 tion of ocean surface waves and the currents (McWilliams et al., 1997)), have

198 been described by Li et al. (2016) and Li and Fox-Kemper (2017). However,  
199 for this study only the standard version of the KPP model is considered.

200 Finally, the OSMOSIS mixed layer model is a new boundary layer model  
201 developed as part of OSMOSIS, and currently undergoing implementation  
202 in NEMO (further details in section 3.6). Like the KPP scheme, turbulent  
203 transports in the OSMOSIS scheme are parameterised using non-local flux-  
204 gradient relationships which are related to the Reynolds budgets for the  
205 turbulent fluxes (Holtslag and Moeng, 1991; Abdella and McFarlane, 1997)  
206 obtained from large-eddy simulation. In the OSMOSIS scheme non-local  
207 flux-gradient relationships are used for both unstable and stable boundary  
208 layers. Unlike the KPP version used here, the OSMOSIS model has been  
209 designed to represent Langmuir turbulence, which has been advocated for in  
210 second-moment closures (e.g., Harcourt, 2013, 2015). The OSMOSIS scheme  
211 does not contain a parameterisation for the effects of shear across the base of  
212 the pycnocline, and there is no contribution of shear-driven mixing in either  
213 the mixed layer or the interior.

### 214 *3.2. Model initiation and setup*

215 All the models are forced at the surface with ECMWF ERA-Interim re-  
216 analysis data (Dee et al., 2011) listed in table 1 and shown in figure 3. ERA-  
217 Interim has a horizontal resolution of  $0.75^\circ$ , or approximately 80 km. We  
218 use data from the closest grid point ( $48.75^\circ$  N,  $16.5^\circ$  W), 23 km from the  
219 centre of the OSMOSIS observations ( $48.7^\circ$  N,  $16.2^\circ$  W). The time resolution  
220 of the surface fluxes is three hours. All models use a 10 minute time step,  
221 and the surface forcing data were linearly interpolated to the same 10 minute  
222 intervals to avoid any differences in how the models treat forcing data which  
223 are more sparse than the model time step.

224 Model performance has been shown to depend on vertical resolution (e.g.,  
225 Large et al., 1994; Acreman and Jeffery, 2007), so here we use a fairly high  
226 vertical resolution of 1 m in every model. The models were all initialised with  
227 the same observed profiles of temperature and salinity collected by glider  
228 SG566 on 24th September 2012, interpolated to the 1 m grid (figure 4). The  
229 models are run from 24th September 2012 to 7th September 2013 (the end  
230 of the observational period) and output variables every hour.

231 All models use Jerlov water type 1B, which is considered to be an appro-  
232 priate water type for the open Atlantic (Simonot and Le Treut, 1986; Stips,  
233 2011). Jerlov water type refers to a set of coefficients that define the double

Parameter	Units
Surface thermal radiation	$\text{W m}^{-2}$
Surface solar radiation	$\text{W m}^{-2}$
Surface sensible heat flux	$\text{W m}^{-2}$
Surface latent heat flux	$\text{W m}^{-2}$
Precipitation	m of water
Wind components at 10 m <sup>+</sup>	$\text{m s}^{-1}$
Coefficient of drag with waves <sup>+</sup>	
2D wave spectra	$\text{m}^2 \text{ s radians}^{-1}$
Surface Stokes drift components*	$\text{m s}^{-1}$

\* Obtained from 2D wave spectra

<sup>+</sup> Surface stress calculated using drag coefficient and wind components

Table 1: Surface forcing parameters from ECMWF ERA-Interim reanalysis data.

234 exponential profile for shortwave radiation absorption (Paulson and Simp-  
 235 son, 1977). In using the same water type for the whole year we are ignoring  
 236 the effect of changes in the optical properties of the water column due to,  
 237 for example, phytoplankton growth. While this may increase differences be-  
 238 tween each model’s output and the observations (Large et al., 1994), this will  
 239 affect all the models similarly so should not invalidate comparisons between  
 240 models. Since not all the models incorporate background diffusion, this is set  
 241 to zero in those models which do include it. All model parameters (except  
 242 background diffusion and Jerlov water type) are set to the default values for  
 243 that model as described in the cited literature. This amounts to a partic-  
 244 ular choice of parameter values for each model and the results might differ  
 245 for other choices, however investigation of the effect of parameter values is  
 246 beyond the scope of this study.

247 SST for each model is the temperature at the first model grid depth, i.e.,  
 248 1 m, comparable to the SST for the glider data which is the median value  
 249 in the uppermost 2 m bin. We calculate MLD for each model based on the  
 250 output profiles of temperature and salinity in exactly the same way in which  
 251 MLD is calculated for the observations, so that we will be comparing like  
 252 with like. However, each model also provides an estimate of the depth of  
 253 active mixing or boundary layer depth, which are described below for each  
 254 model. These will be referred to as the model’s ‘internal’ mixing layer depth  
 255 (IMLD), but note that this is not the same parameter for each model. For the  
 256 TKE and GLS models this is diagnosed from the vertical eddy diffusivity and

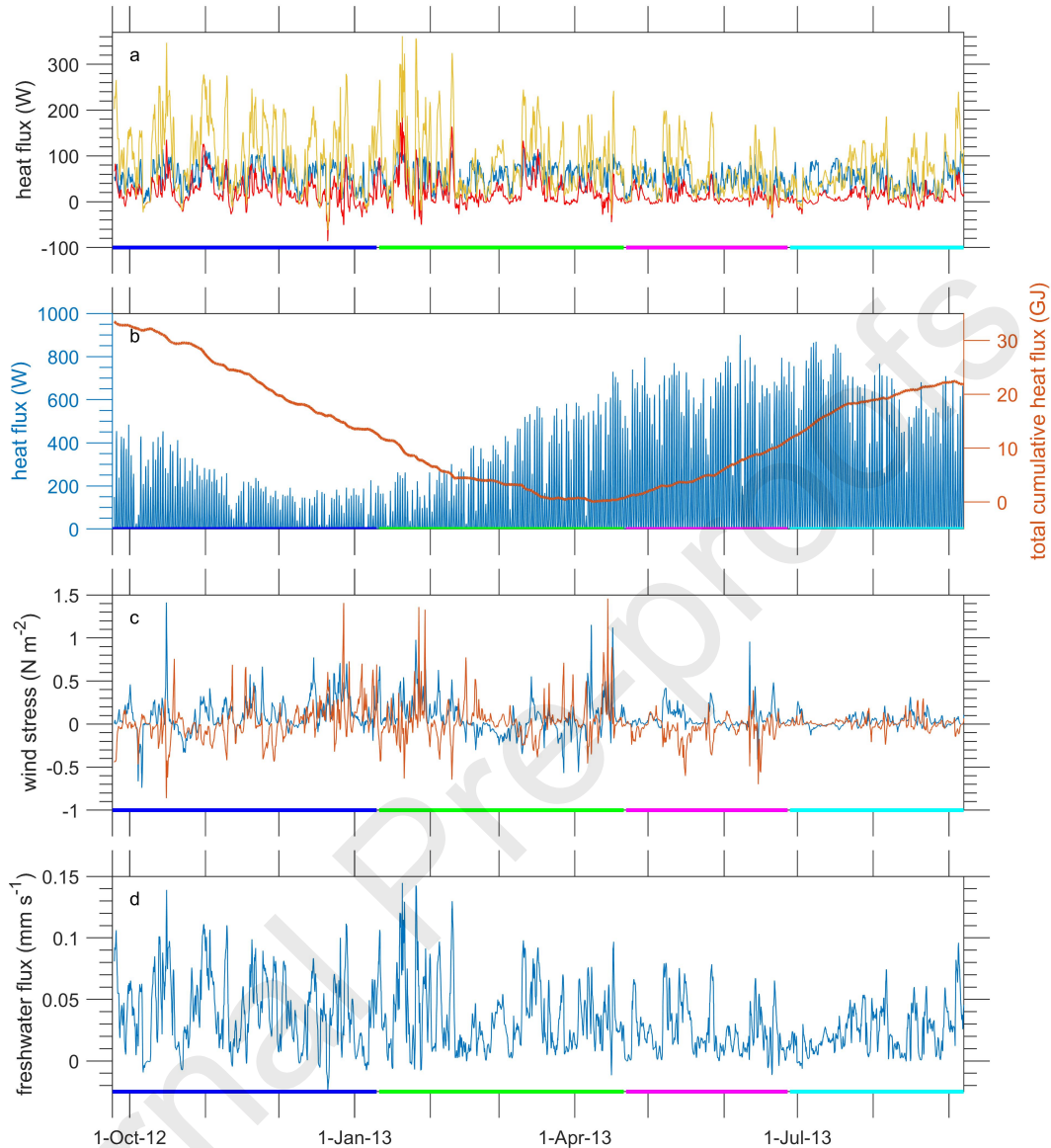


Figure 3: Surface forcing used to drive the models. a) Outgoing surface heat flux, positive upwards. Blue = longwave radiation, red = sensible heat, orange = latent heat. b) Blue = incoming shortwave radiation, positive downwards, red = total cumulative surface heat flux, positive downwards. c) Wind stress. Blue = zonal component, red = meridional component. d) Freshwater flux, i.e., precipitation minus evaporation, positive downwards. The coloured bars at the base of the panels mark the seasons: blue = autumn; green = winter; magenta = spring; cyan = summer.

257 has no impact on the vertical mixing scheme itself, but for the PWP, KPP  
 258 and OSMOSIS models these are length scales that have actual numerical

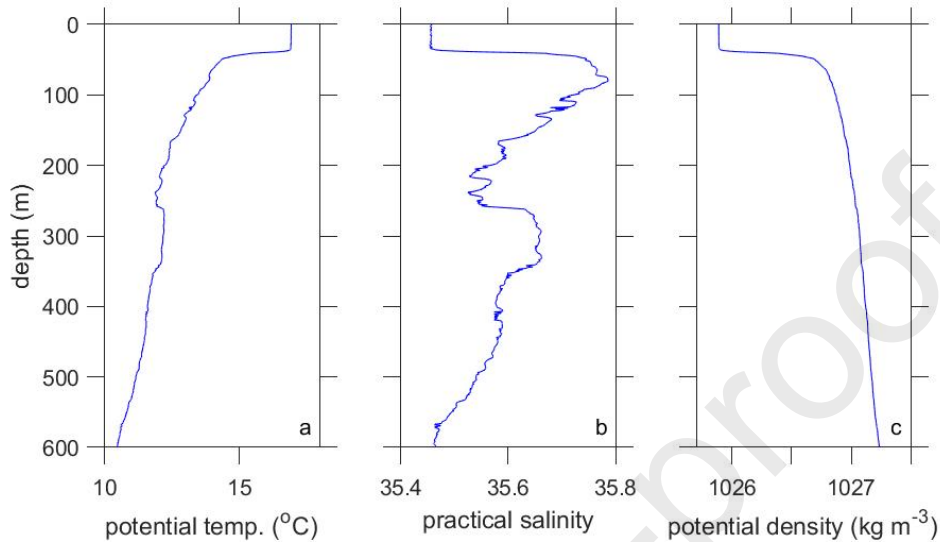


Figure 4: Profiles used to initialize the models: a) potential temperature, b) practical salinity, c) potential density.

259 impacts. All MLDs and IMLDs will be shown as positive downwards.

260 The observational dataset does not include estimates of the depth of  
 261 active mixing, so we are unable to make direct comparisons between an  
 262 observed depth of active mixing and the models' IMLDs. However, one  
 263 would always expect the MLD in the ocean to be greater than or equal to  
 264 the depth of active mixing because properties will be homogeneous at the  
 265 depths where mixing is occurring plus there may be remnant homogeneous  
 266 layers beneath from previous mixing episodes.

267 In model studies the relationship between MLD and IMLD can depend  
 268 on the definition of IMLD used in that model, and on the definition of MLD  
 269 with which it is compared. For example, Large et al. (1994) found boundary  
 270 layer depths (IMLDs in our terminology) in large eddy simulations around  
 271 10% deeper than the mixed layer depth definition they were using (their  
 272 figure 1). However, in the simulations discussed here, each model's IMLD  
 273 was shallower than that model's MLD at all time steps. In other words,  
 274 there is no prima facie reason to expect model IMLD to be deeper than the  
 275 observed MLD. Hence, if a model's IMLD is deeper than the observed MLD  
 276 we can deduce that it must be deeper than the depth of active mixing in the  
 277 real ocean by at least as much as the difference between the model's IMLD  
 278 and the observed MLD. If the model's IMLD is shallower than the observed

279 MLD we do not know how it differs from the depth of active mixing in the  
280 real ocean.

### 281 3.3. PWP

282 The PWP model (Price et al., 1986) was developed to investigate mixed  
283 layer processes in tropical oceans. It is a bulk mixed layer model, which  
284 means that it considers the main driving equations over the entire mixed  
285 layer, and averages the ocean properties (temperature, salinity, and merid-  
286 ional and zonal current velocities) over that layer. The focus is on the param-  
287 eterisation of shear production of turbulent kinetic energy across the base of  
288 the mixed layer and in the pycnocline, which is parameterised through gradi-  
289 ent Richardson number calculations. (Richardson number is a measure of the  
290 relative importance of stratification to destabilizing shear. "Bulk" Richard-  
291 son number is a term used when the Richardson number is calculated over a  
292 slab containing several depth bins, whereas "gradient" Richardson number is  
293 not defined in the mixed layer itself but is calculated in the stratified region  
294 below the mixed layer.) The IMLD is found as the minimum depth required  
295 to keep a bulk Richardson number ( $Ri_b$ ) of a well-mixed layer greater than  
296 a prescribed critical value,  $Ri_b > 0.65$ . This value was determined from field  
297 and laboratory experiments (Price et al., 1978). The model implementation  
298 used originates from Lazarevich and Stoermer (2001), which is a translation  
299 of the original PWP Fortran implementation into Matlab code.

### 300 3.4. KPP

301 The KPP mixed layer model is a turbulence closure scheme model which  
302 uses eddy diffusivity to parameterise small-scale turbulence within the mixed  
303 layer (Large et al., 1994). The model was developed from atmospheric bound-  
304 ary layer models that incorporated nonlocal transport terms in their mixing  
305 parameterisations. The diffusivity is formulated to agree with similarity the-  
306 ory of turbulence in the surface layer and is subject to the conditions that  
307 both it and its vertical gradient match the interior values at the base of the  
308 boundary layer. The diffusivities of the interior mixing processes (internal  
309 waves, shear instability, and double diffusion) are modeled as constants, func-  
310 tions of a gradient Richardson number, and functions of the double-diffusion  
311 density ratio. The IMLD is the minimum of three mixed layer depth defini-  
312 tions: the Ekman depth, the Monin-Obukhov length, and the depth where  
313 the bulk Richardson number exceeds the threshold  $Ri_b > 0.3$  (Large et al.,



1994). An important feature of this model is that the boundary layer allows entrainment into stable stratification below the mixed layer and can produce realistic exchanges of properties between the mixed layer and thermocline. The model script used is a single column of the Multi-Column K Profile Parameterisation ocean model (Hirons et al., 2015), developed by the National Centre for Atmospheric Science at the University of Reading (see [https://puma.nerc.ac.uk/trac/KPP\\_ocean](https://puma.nerc.ac.uk/trac/KPP_ocean)).

### 3.5. TKE and GLS

The TKE and GLS models refer to the 'TKE' and 'GLS' vertical mixing schemes implemented in the NEMO model (Madec, 2008). These schemes are based on the Turbulent Kinetic Energy scheme of Gaspar et al. (1990) and the Generic Length Scale framework of Umlauf and Burchard (2003) respectively, which both belong to the so-called 'Algebraic Stress Model' class of vertical mixing parameterisation (Burchard et al., 2008). This type of parameterisation approximates the turbulent fluxes using the eddy viscosity principle:

$$\begin{aligned}\overline{w'U'} &= -K_M \partial_z \overline{U} \\ \overline{w'T'} &= -K_H \partial_z \overline{T}\end{aligned}\tag{1}$$

where  $U$  is a horizontal velocity component,  $w$  is the vertical velocity component (positive upwards),  $T$  is a tracer, and  $K_M$  and  $K_H$  are respectively the eddy viscosity and eddy diffusivity. The prime and overbar notations represent the fluctuating and time-average components of the quantity respectively (i.e. Reynolds decomposition).  $K_M$  and  $K_H$  have the form:

$$\begin{aligned}K_M &= c_k l_k \sqrt{k} \\ K_H &= c_k^H l_k \sqrt{k}\end{aligned}\tag{2}$$

where  $c_k$  and  $c_k^H$  are dimensionless coefficients or stability functions,  $l_k$  is a mixing length and  $k$  is the turbulent kinetic energy. The calculation of  $c_k$ ,  $c_k^H$ ,  $l_k$  and  $k$  depends on the choice of turbulence closure. In the TKE scheme  $c_k$  and  $c_k^H$  are constant coefficients, and  $k$  is calculated using a prognostic budget equation. In stable stratification  $l_k$  is calculated using the simplified algebraic form suggested by Blanke and Delecluse (1993) where  $l_k \propto N^{-1}$  ( $N$  is the buoyancy frequency), and  $l_k$  is bounded by the distance to the nearest physical boundaries (sea surface and bottom). In unstable stratification where  $N^2 < 0$ ,  $l_k$  is the distance to the nearest physical boundary

344 (sea surface/bottom) or layer of stable stratification. In the GLS framework  
 345  $c_k$  and  $c_k^H$  are complex nonlinear stability functions, and both  $l_k$  and  $k$  are  
 346 calculated using prognostic budget equations. The GLS framework encom-  
 347 passes several well known closures for  $l_k$  and  $k$ , including ' $k - kl$ ' (Mellor and  
 348 Yamada, 1982), ' $k - \epsilon$ ' (Rodi, 1987) and ' $k - \omega$ ' (Wilcox, 1988). Due to the  
 349 number of prognostic equations solved, the TKE scheme and GLS framework  
 350 are examples of 'one-' and 'two-equation' closures respectively.

351 Reffray et al. (2015) explore the performance of the NEMO TKE and GLS  
 352 vertical mixing schemes in a 1D column model case study at Ocean Station  
 353 PAPA. Of the various closures implemented in the GLS framework, they  
 354 find that the ' $k - \epsilon$ ' model gives the best results in terms of temperature and  
 355 salinity biases. Furthermore, they find that the TKE scheme significantly  
 356 understates vertical mixing in the boundary layer and show that an ad-hoc  
 357 parameterisation representing unresolved vertical mixing processes (Rodgers  
 358 et al., 2014) is able to alleviate this. This parameterisation is implemented as  
 359 an additional source of TKE that decays exponentially with depth. Reffray  
 360 et al. (2015) show the TKE scheme to be highly sensitive to the choice of  
 361 e-folding length scale and find that a 10 m length scale (their 'TKE\_10m'  
 362 experiment) gives the best results.

363 We use the 'TKE\_10m' and ' $k - \epsilon$ ' configurations of Reffray et al. (2015)  
 364 as the basis for our TKE ('NEMO TKE') and GLS ('NEMO GLS') simula-  
 365 tions respectively. The reader is referred to Reffray et al. (2015) for more  
 366 details but should note that our simulations use a more recent version of  
 367 NEMO (3.6), although this should have a negligible impact on the results.  
 368 Additionally,  $K_M$  and  $K_H$  are set to an arbitrarily large value wherever static  
 369 instabilities occur to ensure that these are homogenised within a time step.  
 370 This has the effect of reducing the winter MLD by  $\mathcal{O}(10\text{m})$ .

371 For both NEMO simulations the IMLD is taken as the turbocline depth,  
 372 which is the shallowest model depth where  $K_H < 5 \times 10^{-4} \text{ m}^2 \text{ s}^{-1}$ .

### 373 3.6. OSMOSIS model

374 The OSMOSIS scheme combines a bulk model of the surface boundary  
 375 layer (e.g. Kraus and Turner, 1967), which is coupled to a turbulence model  
 376 based on non-local flux-gradient relationships (e.g. Large et al., 1994). The  
 377 bulk model is used to determine the evolution of the depth of the boundary  
 378 layer, and the turbulence model determines the mean profiles within the  
 379 boundary layer, which are represented on a finite difference grid.

380 In unstable conditions the boundary layer is assumed to deepen through  
 381 entrainment. The energy needed to entrain denser water from below the  
 382 boundary layer is assumed to be supplied by a combination of Langmuir tur-  
 383 bulance (McWilliams et al., 1997) and convective turbulence. The equation  
 384 for the depth of the boundary layer is

$$\frac{\partial h_{\text{bl}}}{\partial t} = -\frac{\overline{w'b'_{ent}}}{\Delta B} + \overline{w} \quad (3)$$

385 where  $h_{\text{bl}}$  is the boundary depth,  $\overline{w'b'_{ent}}$  is the buoyancy flux associated  
 386 with entrainment,  $\Delta B$  is the difference between the buoyancy averaged over  
 387 the depth of the boundary layer and the buoyancy just below the base of the  
 388 boundary layer, and  $\overline{w}$  is the large-scale vertical velocity, which is assumed  
 389 to be zero in the integrations presented here. The layer averaged buoyancy  
 390 is obtained by averaging the buoyancies on the model levels, which provides  
 391 the coupling between the bulk and turbulence components of the OSMOSIS  
 392 scheme.

393 The buoyancy flux associated with entrainment is parameterised as

$$\overline{w'b'_{ent}} = -0.03 \frac{w_{*L}^3}{h_{\text{bl}}} - 0.2 \overline{w'b'_0} \quad (4)$$

394 where  $w_{*L}$  is the velocity scale for Langmuir turbulence (Grant and Belcher,  
 395 2009) and  $\overline{w'b'_0}$  is the surface buoyancy flux. The parameterisation of the  
 396 contribution made by Langmuir turbulence to  $\overline{w'b'_{ent}}$  is taken from Grant  
 397 and Belcher (2009).

$$w_{*L} = (u_*^2 u_{s0})^{1/3} \quad (5)$$

398 where  $u_*$  is the surface friction velocity and  $u_{s0}$  is the surface Stokes drift.  
 399 For stable conditions the equation for the depth of the boundary layer is

$$\Delta \tilde{B} \frac{\partial h_{\text{bl}}}{\partial t} = \left( 0.06 + 0.52 \frac{h_{\text{bl}}}{L_L} \right) \frac{w_{*L}^3}{h_{\text{bl}}} + \overline{w'b'_L} \quad (6)$$

400 where  $\overline{w'b'_L}$  is the buoyancy flux averaged over the depth of the boundary  
 401 layer and  $L_L$  is analogous to the Obukhov length (Pearson et al., 2015), and  
 402 is defined as  $L_L = -w_{*L}^3 / 2\overline{w'b'_L}$ . The definition of  $\Delta \tilde{B}$  depends on whether  
 403 the depth of the boundary layer is increasing or decreasing. When  $h_{\text{bl}}$  is  
 404 increasing,  $\Delta \tilde{B} = \Delta B$ , and when  $h_{\text{bl}}$  is decreasing,  $\Delta \tilde{B} = w_{*L}^2 / h_{\text{bl}}$ . The

405 choice for  $\Delta\tilde{B}$  when  $h_{bl}$  is decreasing limits the rate at which the depth of  
 406 the boundary layer can decrease.

407 The layer average buoyancy flux,  $\overline{w'b'_L}$ , is estimated by assuming that the  
 408 sum of the turbulent and radiative heating rates is constant over the depth  
 409 of the boundary layer (Kim, 1976), which gives

$$\overline{w'b'_L} = \frac{1}{2}\overline{w'b'_0} + g\alpha_E \left( \langle I \rangle - \frac{1}{2}(I_0 + I_h) \right) \quad (7)$$

410 where  $\alpha_E$  is the thermal expansion coefficient of sea water,  $\langle I \rangle$  is the solar  
 411 irradiance averaged over the depth of the boundary layer,  $I_0$  is the solar  
 412 irradiance at the surface and  $I_h$  is the solar irradiance at the base of the  
 413 boundary layer.

414 A more complete description of the OSMOSIS scheme can be found at  
 415 [https://forge.ipsl.jussieu.fr/nemo/chrome/site/doc/NEMO/manual/pdf/NEMO\\_manual.pdf](https://forge.ipsl.jussieu.fr/nemo/chrome/site/doc/NEMO/manual/pdf/NEMO_manual.pdf).

#### 416 4. Wavelet analysis methods

417 To investigate variations in the spectral properties of the data, we use the  
 418 wavelet analysis method of Torrence and Compo (1998). Given the number  
 419 of factors which can affect mixed layer properties it was deemed important to  
 420 use an analysis method which could pick out significant periodicities which  
 421 are only present for a portion of the total record, because such periodicities  
 422 might not be identified in power spectra of the whole time series.

423 The time series of observed SST and MLD were first linearly interpo-  
 424 lated to regular 4-hourly intervals, and the output from each model was  
 425 sub-sampled to the same 4-hourly intervals. (This sub-sampling does not  
 426 make a significant difference to the results presented.) We chose to use 4-  
 427 hourly intervals because although the gliders obtain profiles roughly every  
 428 2 hours, they are not regularly spaced in time. Due to the "V" shape of  
 429 glider movement, each upcast and next downcast are separated by only a  
 430 few minutes near the surface, with a wait of nearly 4 hours until the next  
 431 pair. Similarly near the bottom of the profile each downcast and next upcast  
 432 are closely spaced in time with a wait of nearly 4 hours until the next pair.  
 433 It is only around the middle of the profiling depth that data is obtained at  
 434 approximately regular 2-hourly intervals. Hence 4 hours was considered a  
 435 more appropriate interpolation interval.

436 Because the distributions of SST and MLD are distinctly non-normal,  
 437 we transform all the time series into records of percentiles (in terms of their

438 cumulative distribution function), thus forcing the probability density func-  
 439 tions to be rectangular (Grinsted et al., 2004). The resulting time series  
 440 are padded with zeros to avoid wraparound effects and the wavelet power  
 441 spectra calculated using a Morlet wavelet. Significance is determined by  
 442 comparison with a theoretical red-noise spectrum calculated from the lag-1  
 443 autocorrelation coefficient for each time series. The null hypothesis is defined  
 444 for the wavelet power spectrum as follows (Torrence and Compo, 1998): it  
 445 is assumed that the time series has a mean power spectrum (the theoretical  
 446 red-noise spectrum, given in equation 8); if a peak in the wavelet power spec-  
 447 trum is significantly above this background spectrum, then it can be assumed  
 448 to be a true feature with a certain percent confidence.

$$P_k = \frac{1 - \alpha^2}{1 + \alpha^2 - 2\alpha \cos(2\pi k/N)} \quad (8)$$

449 where  $P_k$  is the mean power spectrum,  $k = 0, 1 \dots N/2$  is the frequency  
 450 index,  $\alpha$  is the lag 1 autocorrelation coefficient, and  $N$  is the number of  
 451 values in the time series. Wavelet spectra of the total surface heat flux and  
 452 wind speed were calculated in the same way, except that the time series were  
 453 not transformed into records of percentiles because the distribution of these  
 454 variables was approximately normal.

455 To further investigate the relationships between different time series, we  
 456 calculate wavelet coherence following the methods of Torrence and Webster  
 457 (1999), using the code made available by Grinsted et al. (2004). Wavelet  
 458 coherence can be thought of as the localized correlation coefficient in time  
 459 frequency space; it shows whether non-stationary time series are co-varying  
 460 at a particular frequency (but not at other frequencies) and at a particular  
 461 time (but not throughout the entire record). This analysis method was cho-  
 462 sen because simple correlations or coherence tests over the entire time series  
 463 might not identify the relationships which the wavelet coherence method ex-  
 464 poses. Significance is determined using Monte Carlo methods as detailed by  
 465 Grinsted et al. (2004). Note that the annual relationship between surface  
 466 forcing and mixed layer properties (cooling and deepening in autumn, warm-  
 467 ing and shoaling in spring) will not appear significant because the time series  
 468 are too short. Hence the strong correlation between SST and cumulative  
 469 net surface heat flux found by Damerell et al. (2016) will not be apparent  
 470 because it was largely a consequence of the strong annual cycle. Multi-year  
 471 time series would be required for the annual cycle to appear significant in  
 472 this wavelet analysis.

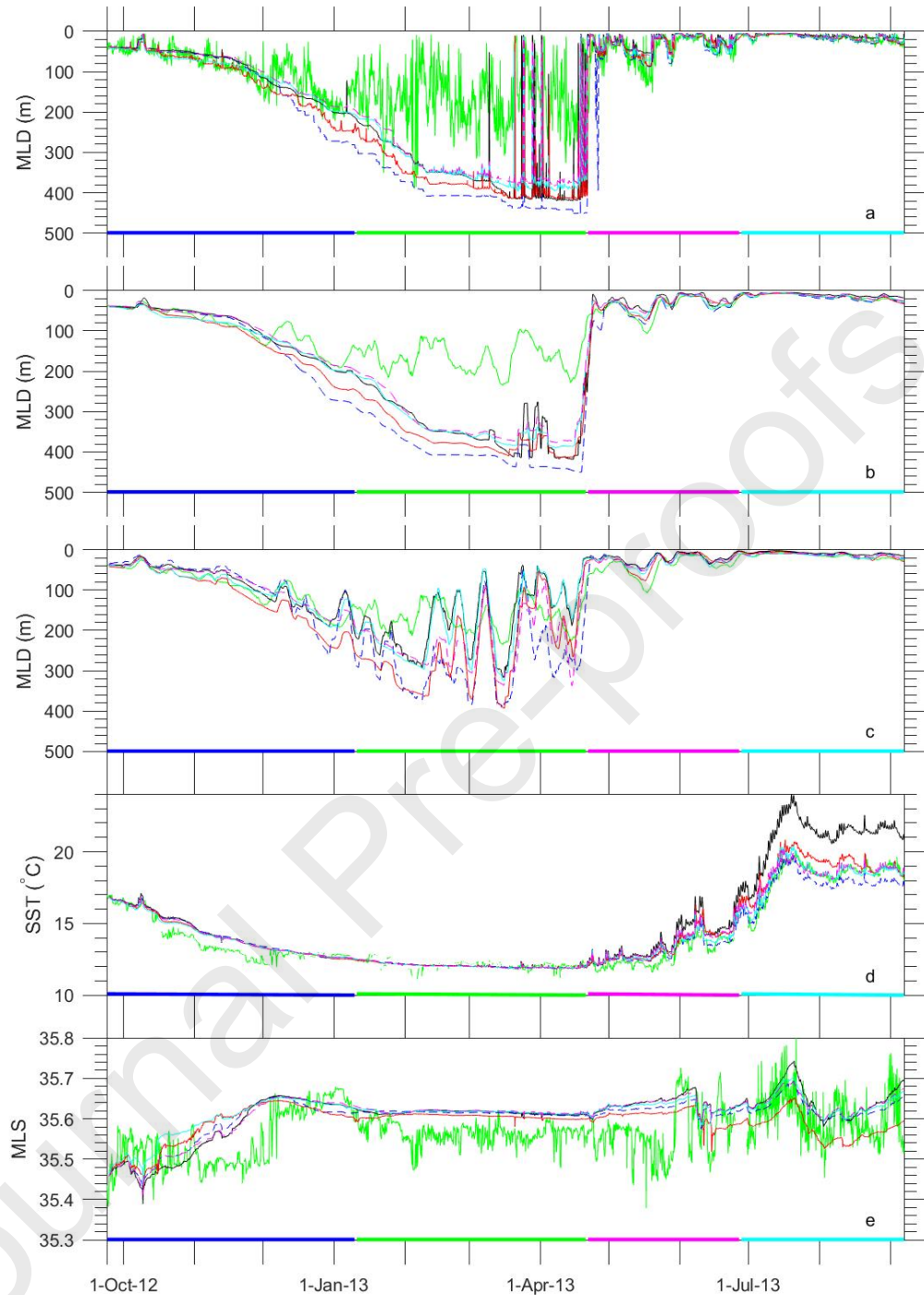


Figure 5: Mixed layer and sea surface properties over the year of the OSMOSIS field campaign, from both the glider observations and the models. a) MLD. b) MLD smoothed by applying a 5-day running mean as in section 2; this is shown for clarity only and is not used in the analysis. c) Observed MLD and models' internal MLDs, all smoothed by applying a 5-day running mean as in panel b). d) SST. e) MLS. In all panels, green line = glider observations, dashed blue line = PWP, cyan line = NEMO GLS, dashed magenta line = NEMO TKE, black line = KPP, red line = OSMOSIS model. The coloured bars at the base of the panels mark the seasons: blue = autumn; green = winter; magenta = spring; cyan = summer.



473 **5. Results and Discussion**474 *5.1. SST overview*

475 All the models output SSTs which are broadly representative of the ob-  
 476 served time series (figure 5d). The annual cycle of cooling during autumn, a  
 477 fairly constant temperature over the winter, then warming to a peak in July  
 478 is seen clearly in all the models. Seasonal mean biases in each model are less  
 479 than 1°C (table 2), similar to the model/observation differences found by  
 480 Lazarevich et al. (2004), except that KPP is considerably warmer than the  
 481 observations in summer. This suggests that the drivers of SST variability in  
 482 this region are largely 1-dimensional, unlike at OSP where advective effects  
 483 are considered important in the winter (Large et al., 1994).

model	observed			model bias		
	SST	PWP	NEMO GLS	NEMO TKE	KPP	OSMOSIS
Autumn	13.75	0.48	0.37	0.45	0.47	0.39
Winter	12.12	-0.05	-0.07	-0.06	-0.06	-0.07
Spring	12.87	0.29	0.51	0.67	0.97	0.58
Summer	18.15	-0.40	0.22	0.30	2.91	0.74
whole year bias		0.11	0.24	0.31	0.91	0.36
rms difference		0.57	0.52	0.60	1.48	0.66

Table 2: Seasonal mean observed SST, and seasonal biases between each model and observed SST (°C). Positive bias = model SST warmer than observed SST.

484 The distribution of observed SST is bimodal (figure 6a) with a large peak  
 485 at a temperature of 12°C. This is due to the period from early February until  
 486 late May when the SST remains nearly constant at around 12°C. The average  
 487 winter SST of 12.12°C (table 2) is slightly cooler than the winter SSTs of  
 488 12.14°C (2003), 12.25°C (2004) and 12.61°C (2005) found by Hartman et al.  
 489 (2010) at the PAP-SO. None of the models reproduce the coldest SSTs seen  
 490 in the observations, which reach a minimum of 11.1°C. GLS, TKE and KPP  
 491 reach a minimum temperature of 11.8°C and PWP and OSMOSIS reach  
 492 a minimum of 11.9°C. However, it is clear (figure 5d) that this is because  
 493 the models show less variability in winter SSTs than the observations. The  
 494 average winter SST is in fact slightly cooler in each model (table 2) than in  
 495 the observations (between 0.05 and 0.07°C cooler).

496 The second, smaller peak of the bimodal distribution (figure 6 and figure  
 497 5d) is due to the period in late July and August when the SST again remains

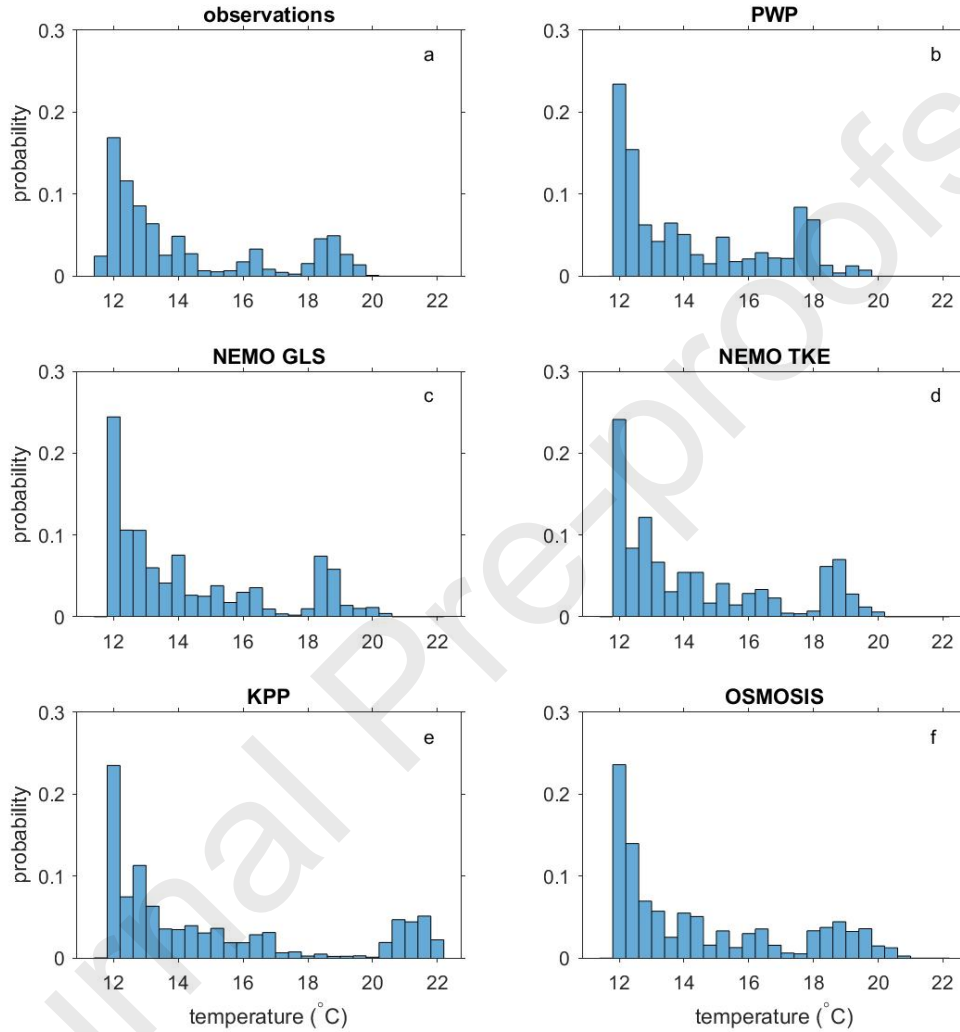


Figure 6: Histograms of SST for the observations and for each model. These are shown as probabilities, i.e., the height of the bar equals the number of counts in that bin divided by the total number of data points for that variable.

498 nearly constant around 18 - 19°C, consistent with the summer SSTs reported  
 499 by Hartman et al. (2010). PWP, GLS, TKE and OSMOSIS have summer  
 500 temperature biases between -0.40 and 0.74°C, but it is only KPP which really  
 501 differs from the observations, with a mean bias in the summer of 2.9°C (table

2), similar to the summer SST bias in KPP seen by Acreman and Jeffery (2007). KPP also has the largest warm bias in spring ( $0.97^{\circ}\text{C}$ ). We postulate that this is related to differences in MLD/IMLD: KPP has the shallowest MLD and IMLD in the spring and summer (table 4) which will tend to trap heat in the mixed layer. TKE, in particular, has similar MLD biases to KPP (though not quite as shallow in spring and summer), but KPP's IMLD is considerably shallower than TKE's in spring and summer. Unlike TKE, where the IMLD is purely diagnostic, KPP's IMLD has an impact on model physics so may be a factor in KPP's SST bias in spring and summer.

Burchard and Bolding (2001) compared two 1D TC schemes with observations at OSP and found a shallow MLD bias in summer, which we estimate to be around 10 m from their figure 18. They attribute this to either erroneous surface fluxes or strong advective effects. However, they also comment that one model's predicted MLD is shallower than the other's, leading to warmer summer SSTs in that model. We estimate from their figure 18 that the difference in MLD is perhaps around 2 m, and the difference in SST around  $0.3^{\circ}\text{C}$ . This illustrates that during the summer when the mixed layer is shallow, relatively small differences in MLD can produce quite significant differences in SST.

PWP is unusual in exhibiting a cold bias in the summer. Archer et al. (1993) compared PWP simulations with observations at OSP over a 6-year period and also found cold biases in model summer SSTs of a similar magnitude to those seen here, as did Lazarevich et al. (2004) in their comparisons of PWP with float-observed temperatures and NCEP reanalysis SSTs in the north Atlantic. Archer et al. (1993) suggest that this may be due to small inaccuracies in the surface heat fluxes, but that seems unlikely here since the other models all have warm SST biases in summer.

## 5.2. *Mixed layer salinity*

The models do not do a very good job of reproducing the observed MLS (figure 5e and figure 7), though this is not entirely unexpected (section 1). In particular, they fail to capture the short term variability over periods of hours to days. Only some large-scale changes are captured, notably the increase in MLS in mid-July when the mixed layer is extremely shallow and high temperatures are leading to large surface evaporation (see also the large latent heat flux in July despite low wind speeds in figure 3). The distribution of the observed MLS (figure 7a) is approximately a wide Gaussian, with a mean of 35.57 and a large standard deviation of 0.06. The distributions are

539 much narrower for all the models and are shifted towards higher salinities,  
 540 with only a small tail of values at the lower end. OSMOSIS has a mean  
 541 MLS of 35.59 (closest to the observations), PWP, KPP and TKE have a  
 542 mean MLS of 35.61 and GLS a mean of 35.62, considerably higher than the  
 543 observed mean of 35.57. OSMOSIS has the smallest bias in all seasons except  
 544 the autumn (table 3). However, it is worth noting that the lower annual bias

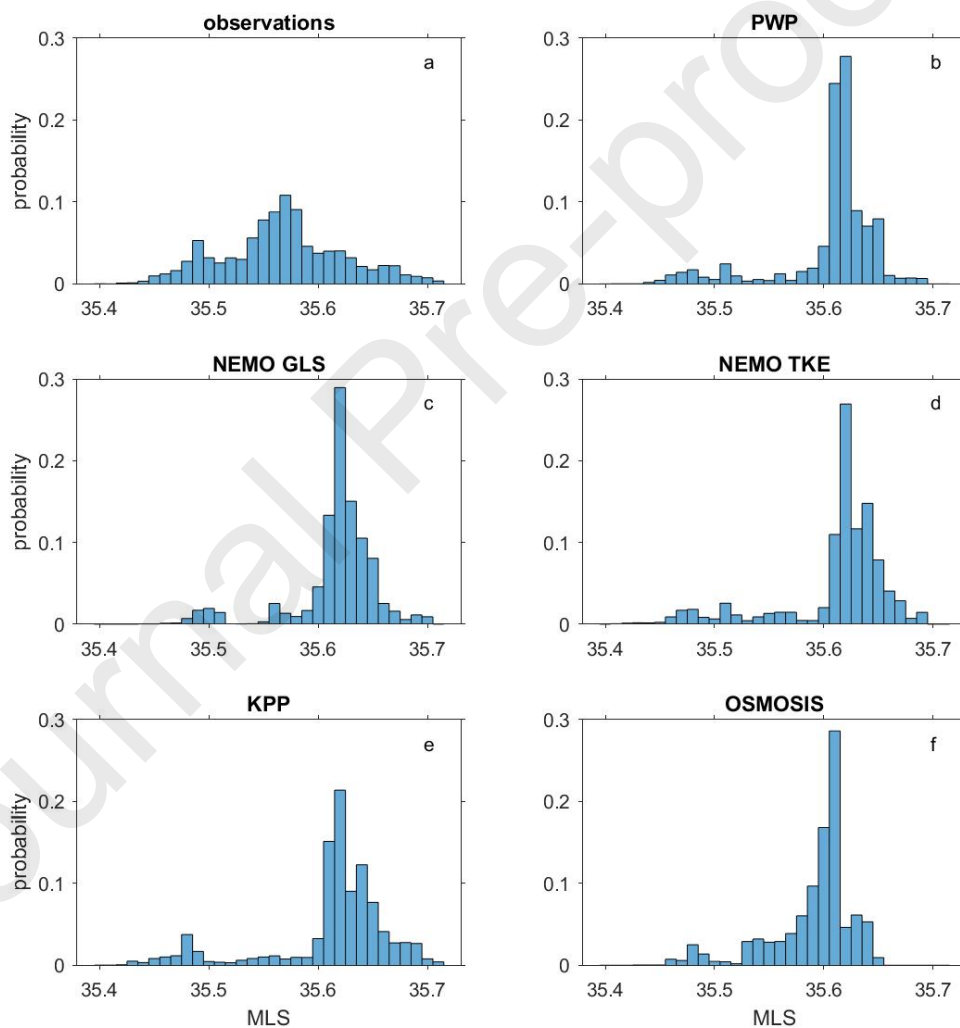


Figure 7: Histograms of MLS for the observations and for each model, shown as probabilities as in figure 6.

545 achieved by OSMOSIS is largely because it has both positive and negative  
 546 biases which cancel out to some extent; the rms difference between OSMOSIS  
 547 and the observations is only slightly smaller than for the other models. The  
 548 annual average biases in MLS (table 3) of 0.02 to 0.05 represent 6-14% of  
 549 the range in observed MLS over this year. When comparing the model-  
 550 observation agreement of MLS and SST (e.g., figure 5), it is worth bearing in  
 551 mind that the range in SST is determined by a very large scale process, i.e.,  
 552 the annual cycle in surface heat flux. Without a similar driver of large annual  
 553 change in MLS, small variations can appear more significant than they really  
 554 are. However, as will be discussed in section 5.3, the salinity biases here are  
 555 large enough to produce significant density biases.

	observed		model bias			
	MLS	PWP	NEMO GLS	NEMO TKE	KPP	OSMOSIS
Autumn	35.55	0.02	0.04	0.02	0.02	0.03
Winter	35.57	0.05	0.05	0.05	0.05	0.04
Spring	35.57	0.05	0.06	0.07	0.07	0.04
Summer	35.60	0.03	0.04	0.04	0.05	-0.02
whole year bias		0.04	0.05	0.04	0.04	0.02
rms difference		0.07	0.07	0.07	0.07	0.06

Table 3: Seasonal mean observed MLS, and seasonal biases between model and observed MLS (psu). Positive bias = model MLS greater than observed MLS.

556 Model MLS is dependent on the surface fluxes of precipitation and latent  
 557 heat (from which evaporation is calculated). These fluxes can be very local-  
 558 ized and are difficult to measure and model consistently (e.g., difficulties in  
 559 modelling cloud cover), so it is not surprising that MLS derived from reanal-  
 560 ysis surface flux products is not very similar to observed values. Moreover  
 561 the localized nature of these fluxes means MLS can vary considerably in the  
 562 horizontal, leading to variability in observed MLS due to advection which is  
 563 obviously not present in a 1D model.

564 It is worth noting, however, that local differences in MLS in this region  
 565 are unlikely to have a large influence on large scale climate modelling because  
 566 MLS does not directly affect the atmosphere in the same way that SST does.  
 567 Biases in MLS over a wide area and long time scales might be important  
 568 since these would affect water mass formation and circulation, but that is  
 569 beyond the scope of this paper.

570 *5.3. Mixed layer density*

571 The study region is a region where Eastern North Atlantic Central Water  
572 (ENACW) forms during the winter (Pollard and Pu, 1985; Pollard et al.,  
573 1996). The slightly cooler SSTs and slightly higher MLSs (tables 2 and 3)  
574 in winter would lead to the formation of a higher density water mass than  
575 that found in the real ocean, which could have implications for the wider  
576 circulation.

577 We estimate equivalent density biases by calculating density for the ob-  
578 served average winter temperature of 12.12°C and salinity of 35.57, then  
579 subtracting(adding) the winter temperature(salinity) bias for each model and  
580 recalculating density. The winter temperature biases in table 2 lead to den-  
581 sity biases of approximately +0.01, and the winter salinity biases in table  
582 3 lead to density biases of approximately +0.04. The combined biases (i.e.,  
583 calculating density using both the temperature and salinity biases) amount  
584 to an increase in density of approximately 0.05. Since the ENACW of sub-  
585 tropical origin found beneath the surface mixed layer in this region (Damerell  
586 et al., 2016) is found at  $\sigma_\theta$  in the range 27 to 27.2 (Harvey, 1982), a density  
587 bias of 0.05 is not insignificant. However, as will be discussed in section 5.4,  
588 the wintertime density biases do not seem to impact negatively on the spring  
589 restratification and subsequent development of the MLD and SST.

590 *5.4. MLD overview*

591 The observed MLDs (figure 5a, b) are broadly consistent with previous  
592 observations in this area (e.g., Hartman et al., 2015; Henson et al., 2012;  
593 Martin et al., 2010; Steinhoff et al., 2010; Hartman et al., 2010), taking into  
594 account the varying MLD definitions used in different studies. Henson et al.  
595 (2012) consider differences in monthly mean MLD in years with positive  
596 or negative North Atlantic Oscillation (NAO) index in winter. They used  
597 the Hadley Centre’s EN3 objectively analysed temperature and salinity data  
598 from 1959 to 2009, and calculated MLD as the depth at which a density  
599 difference of 0.03 kg m<sup>-3</sup> from the surface was observed. The composite MLD  
600 for positive NAO years reached a maximum of 280 m in March, whereas in  
601 negative NAO years it reached only 170 m. They relate this to the greater  
602 wind stress in positive NAO years, resulting in increased mechanical mixing.  
603 Our results are in agreement, with an average winter mixed layer depth of  
604 165 m (table 4) and weakly negative winter NAO index in 2013.

605 Winter MLD has been shown to be an important driver of nitrate flux  
606 into the surface mixed layer (Hartman et al., 2010; Steinhoff et al., 2010).



607 Temporary shoaling of the MLD during winter and spring may therefore  
 608 influence nutrient fluxes. In this region, the winter shoaling of the MLD ap-  
 609 pears to be linked to sporadic short-lived chlorophyll blooms observed during  
 610 OSMOSIS in winter, well before the main spring bloom event in June (Erick-  
 611 son and Thompson, 2018; Binetti et al., this issue; Rumyantseva et al., this  
 612 issue). Previous studies have used data from Argo floats, XBTs, CTDs and  
 613 moorings over a wide area (45°N to 52°N and 26.08°W to 8.92°W, excluding  
 614 the shelf area) around the PAP-SO to estimate MLDs (Hartman et al., 2010,  
 615 2015). In all the years considered, those estimates showed MLDs increas-  
 616 ing fairly smoothly from September to the time of maximum depth (which  
 617 varied from January to March), and then decreasing again to the summer  
 618 minimum. This differs from the pattern observed here where the mean MLD  
 619 remained approximately constant over the winter (167, 161 and 163 m in  
 620 January, February and March respectively) but with high variability. (For  
 621 example, compare our figure 5b with Hartman et al. (2010) figure 4b and  
 622 Hartman et al. (2015) figure 3b.) The winter time range of MLD observed  
 623 by the gliders was 11 m to 378 m. This high variability in MLD is likely to  
 624 be significant for nutrient fluxes and winter blooms (Hartman et al., 2010;  
 625 Steinhoff et al., 2010; Erickson and Thompson, 2018; Binetti et al., this issue;  
 626 Rumyantseva et al., this issue).

627 Model MLDs are broadly representative of the observed MLDs (figure 5a  
 628 and b) except in winter when the model MLDs are too deep, with winter  
 629 average biases between 160 and 228 m (table 4), and do not exhibit the same  
 630 variability as the observations. This can be partially explained by the fact  
 631 that in this region there is considerable submesoscale activity in winter, which

model	observed			model bias		
	MLD	PWP	NEMO GLS	NEMO TKE	KPP	OSMOSIS
Autumn	91	25(-3)	12(1)	2(-6)	7(-5)	25(23)
Winter	165	228(104)	169(16)	160(59)	173(7)	198(82)
Spring	42	-3(-21)	-11(-15)	-16(-15)	-17(-21)	-10(-15)
Summer	15	1(-5)	0(-1)	-3(-1)	-5(-7)	0(-2)
whole year bias		74(24)	51(2)	44(12)	48(-5)	64(28)
rms difference		137(106)	105(73)	102(74)	110(79)	121(90)

Table 4: Seasonal mean observed MLD, and seasonal biases between model and observed MLD (m). Figures in brackets are mean differences between each model’s IMLD and the observed MLD. Positive bias = model MLD/IMLD deeper than observed MLD.

632 will tend to restratify the mixed layer (Thompson et al., 2016). This subme-  
633 soscale activity is not present in these one dimensional models. Viglione et al.  
634 (2018) find a similar result when comparing MLDs from a 1D PWP model  
635 with observations in Drake Passage: the lack of submesoscale instabilities in  
636 the model results in MLDs which are too deep and insufficiently variable.  
637 The models' IMLDs are also deeper than the observed MLD in winter, indi-  
638 cating that they are likely to be deeper than the depth of active mixing in the  
639 real ocean. The winter-time difference between model IMLD and observed  
640 MLD is smallest for KPP and GLS (table 4) but this is largely because they  
641 are too deep at the start of winter and become shallower than the observed  
642 MLD towards the end of winter (figure 5c) and these differences cancel out,  
643 whereas for PWP and OSMOSIS, the winter-time IMLDs remain consistently  
644 too deep giving a greater average difference with the observations.

645 It is noticeable, however, that all the model IMLDs reproduce the ob-  
646 served wintertime shoaling and deepening of the MLD much better than the  
647 model MLDs (figure 5b, c), as well as having smaller average differences in  
648 winter (table 4). As discussed above, this temporary shoaling may be sig-  
649 nificant for fluxes of nitrates into the mixed layer in winter, so model IMLD  
650 may be more useful for understanding winter bloom dynamics than MLD  
651 calculated in the manner used for observations.

652 The general pattern is that in autumn and winter, model MLDs are deeper  
653 than the observed MLDs, whereas in spring and summer the model MLDs are  
654 shallower than observed MLDs. The shallow biases in spring and summer  
655 will result in a 'trapping' of surface forcing effects, i.e., the effects of the  
656 surface forcing will tend not to reach as deep as they should. This will affect  
657 the ability of these models to reproduce summer water mass formation, air-  
658 sea fluxes, and bloom dynamics through the interaction between mixed layer  
659 depth and nutrient fluxes.

660 All the models reproduce the observed spring restratification, though one  
661 or two days later than in the observations (table 5). One would generally  
662 expect the depth of active mixing to shoal before the mixed layer depth, and  
663 indeed each model's IMLD shoals several days earlier than that model's MLD.  
664 However, we could not find any observations in this region in the literature  
665 which indicate how much earlier one would expect the depth of active mixing  
666 to shoal than the MLD, so we are unable to comment on which model's IMLD  
667 behaves most like the real ocean.

668 It is noticeable that the biases in MLD are fairly small in spring and  
669 summer despite the preceding large biases in winter MLD and the winter

	observations	PWP	NEMO GLS	NEMO TKE	KPP	OSMOSIS
MLD	21	23	22	22	23	23
IMLD		21	17	19	17	19

Table 5: Date (in April 2013) of spring restratification of the MLD for the observations, and date of spring restratification of the MLD and IMLD for each model. Model dates are calculated in the same way as for the observations, as described in section 2.

670 mixed layer density biases (which are largely due to biases in MLS (section  
671 5.2)). Large et al. (1994) compared KPP with observations at OSP, and also  
672 found that the spring restratification reduced biases in MLD. However, their  
673 simulation was initialised on 15th March, only about a month before the  
674 spring restratification, and the initial MLD bias was only about 15 m. Here  
675 the spring restratification removes much larger MLD biases.

676 The spring and summer MLD biases are not correlated with the winter  
677 MLD or MLS biases (tables 3 and 4). Similarly, the spring and summer SST  
678 biases are not correlated with the winter MLD or MLS biases (tables 2, 3  
679 and 4). The surface forcing generating the spring restratification appears  
680 to be a sufficiently dominant process that preceding biases are unimportant.  
681 This suggests that when using a 1D model in a similar ocean environment  
682 (mid-latitudes away from topography) it may be acceptable to initialize the  
683 model using a relatively low resolution profile (e.g., from an Argo float) in late  
684 winter when stratification is low, and simply allow the model to generate the  
685 spring stratification, rather than requiring a higher resolution profile (capable  
686 of resolving a steep pycnocline) suitable for initializing during the spring or  
687 summer.

### 688 5.5. Diurnal cycles

689 All the models show some evidence of a diurnal cycle in SST (figure 8),  
690 significant at the 95% confidence level, starting in March and continuing to  
691 the beginning of September. The surface forcing which drives the models  
692 also shows a significant diurnal cycle in total surface heat flux from March to  
693 September (figure 9a), and all the model SSTs show evidence of a coherent  
694 relationship with the cumulative total surface heat flux at a diurnal timescale  
695 for much of the year (figure 10), though this is more obvious from mid-  
696 February onwards than in the autumn and early winter.

697 This diurnal cycle is not, however, as significant in the observed SSTs  
698 as in the model SSTs (figure 8), and the observations also show much less

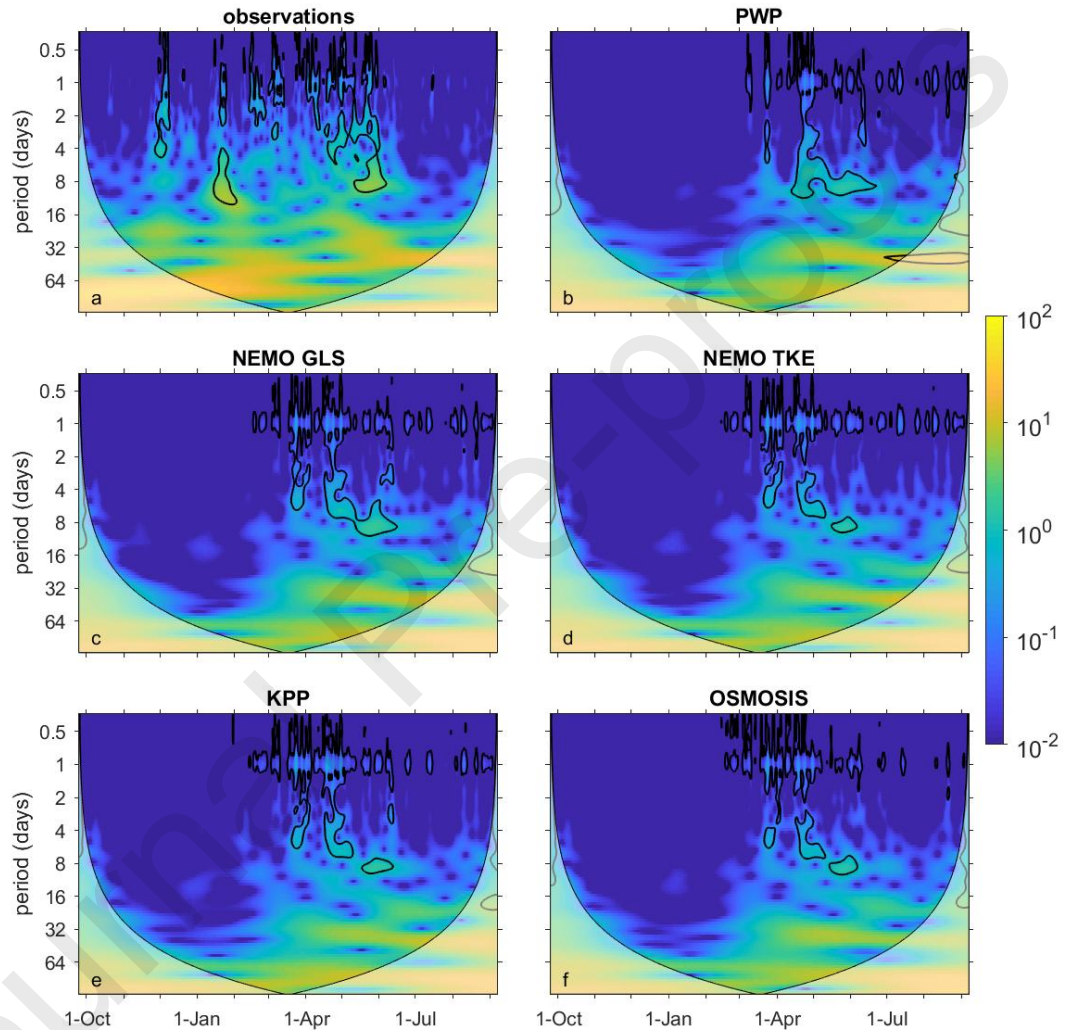


Figure 8: Wavelet spectra of SST for the observations and for each model. In each panel, the black contours enclose regions of greater than 95% confidence level calculated using the corresponding red-noise spectrum as the null hypothesis (see text). The shaded regions on either end indicate the cone of influence, where edge effects become important and results should be viewed with caution.

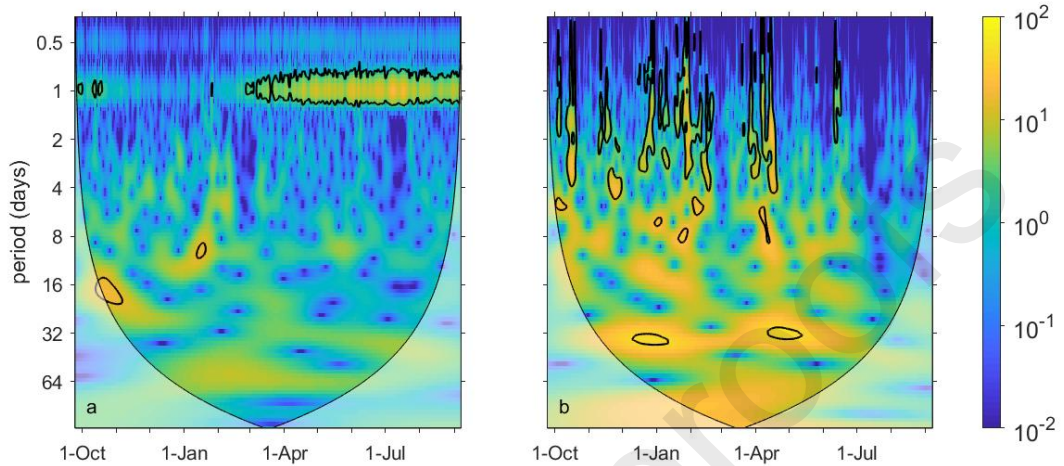


Figure 9: Wavelet spectra of the surface forcing: a) total surface heat flux, b) wind stress. Otherwise as figure 8.

699 coherence with the surface heat flux (figure 10). In the real ocean the diurnal  
 700 cycle may be masked by noise from other ocean processes not present in the  
 701 models, such as the influence of advection, internal waves and submesoscale  
 702 processes, and from the fact that the glider is not sampling in one location.  
 703 Biases or missing processes in the surface forcing may also lead to discrep-  
 704 ancies between the observed and modelled SSTs. For example, Giglio et al.  
 705 (2017) have recently demonstrated the significance of wind gusts in regulat-  
 706 ing how fast surface water is mixed to greater depths when daily mean winds  
 707 are weak, and the reanalysis wind stress used to drive the models will not  
 708 include wind gusts in a realistic fashion. Moreover, cloud cover is known to  
 709 be difficult to model and this will lead to discrepancies between the reanal-  
 710 ysis surface heat flux driving the models and the surface heat flux affecting  
 711 the real ocean (Taylor, ed.; Large and Yeager, 2009). For example, reduced  
 712 cloud cover during the spring and summer will tend to lead to increased heat  
 713 flux into the ocean during the day, and increased heat flux out of the ocean at  
 714 night. This would increase the magnitude of the diurnal cycle of SST in the  
 715 models as compared with the observations. All these factors could lead to a  
 716 much reduced diurnal cycle in the observations compared with the models.

717 As with SST, we again see a significant relationship between MLD and  
 718 the cumulative surface heat flux at diurnal time scales (figure 11), though  
 719 this is not as pronounced as for SST. This relationship is again considerably



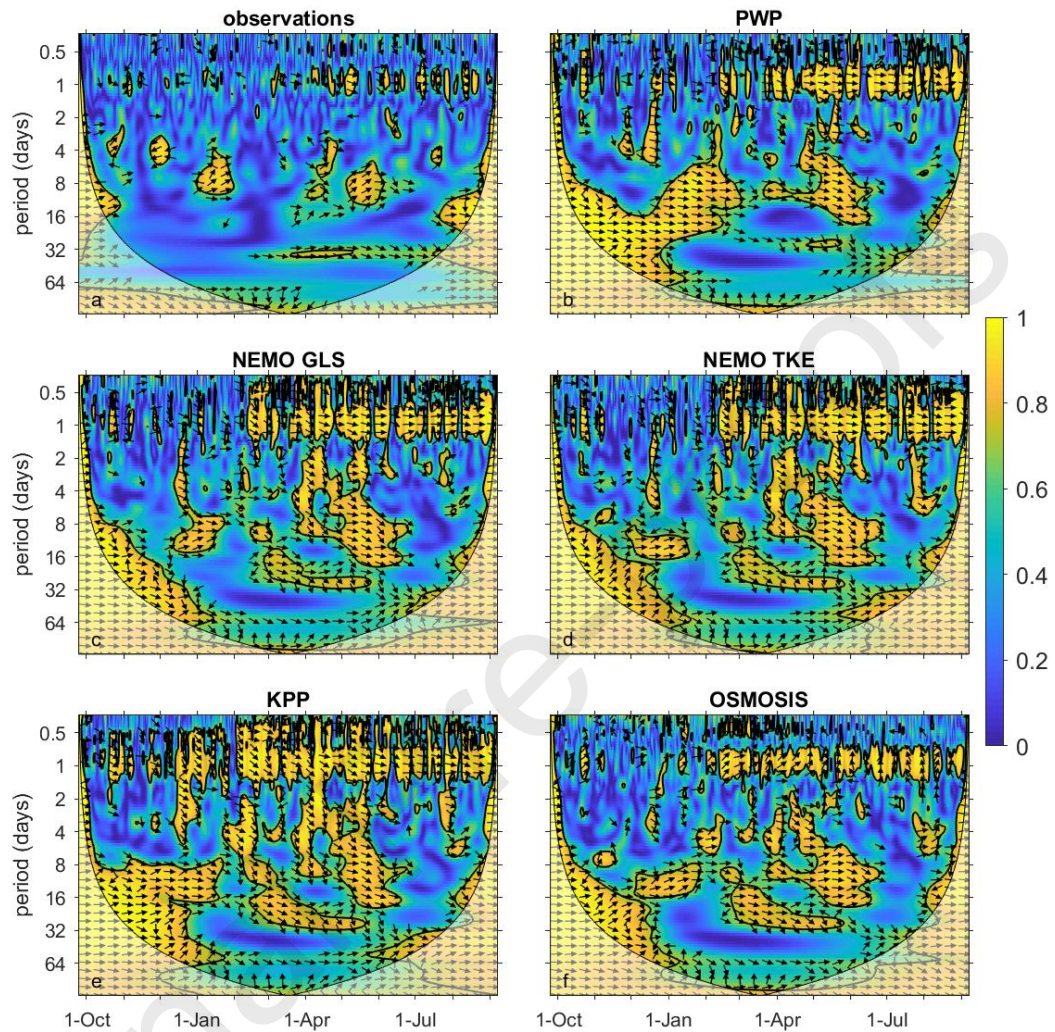


Figure 10: Wavelet coherence for SST and cumulative total surface heat flux. In each panel, the black contours enclose regions of greater than 95% confidence level calculated using Monte Carlo simulations (see text). The shaded regions on either end are as in figure 8. The arrows represent the relative phase - arrows pointing to the right imply the time series are in phase, arrows pointing left imply anti-phase, arrows pointing straight up imply the surface heat flux leads SST by a quarter of a cycle. Note that this indication of lag in all wavelet coherence figures is relative to the length of the cycle. For example, an arrow pointing up and right at an angle of  $45^\circ$  refers to a lag of an eighth of a cycle - e.g., arrows pointing up and right at  $45^\circ$  in this figure mean SST lags the surface heat flux by one day for a cycle with an 8-day period but by 4 days for a cycle with a 32-day period.



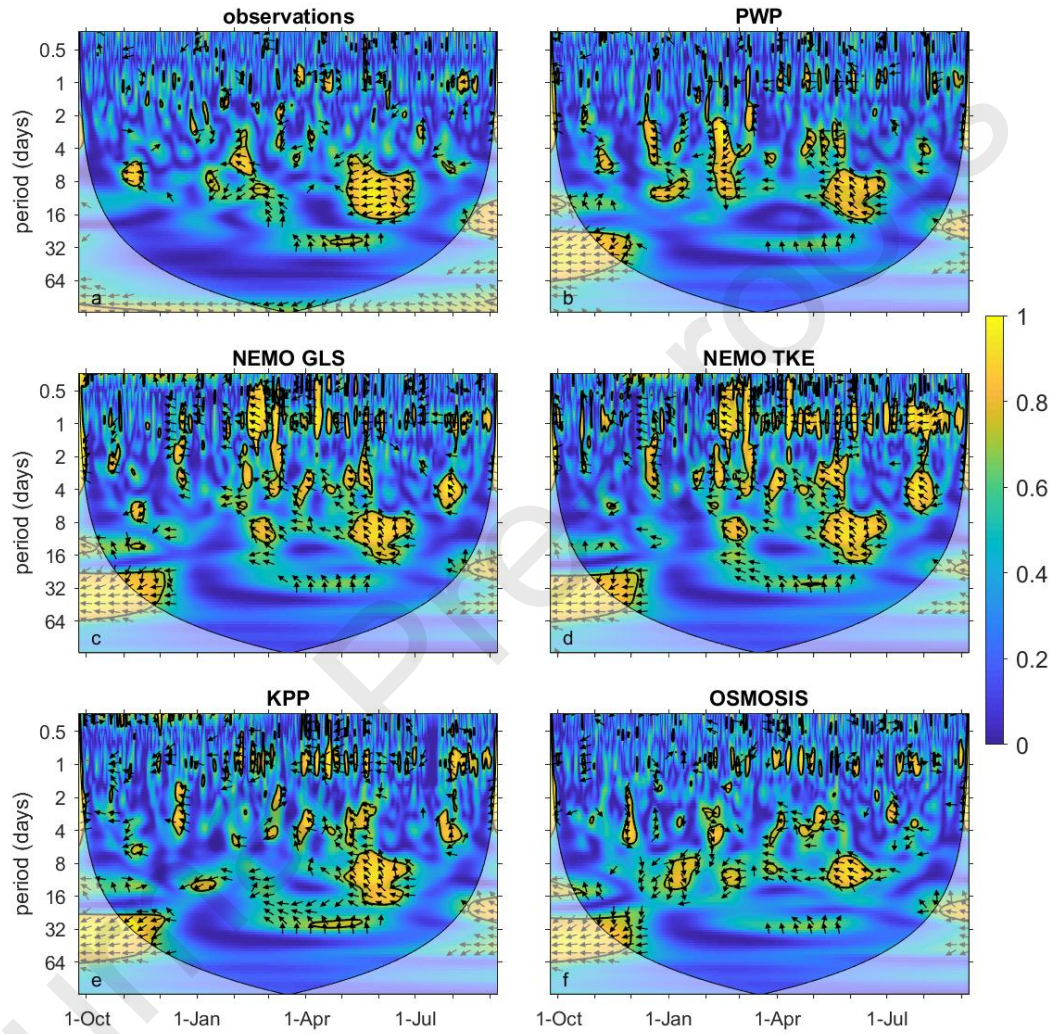


Figure 11: Wavelet coherence for MLD and cumulative surface heat flux. Otherwise as in figure 10.

720 more present in the models than in the observations. The MLD and surface  
721 heat flux are in approximate anti-phase, as one would expect (i.e., surface  
722 heat flux increases, MLD shoals). With solar radiation incoming during the  
723 day the SST warms and the mixed layer shoals due to thermal stratification.  
724 At night the ocean loses heat to the atmosphere, convection occurs, the SST  
725 decreases and the MLD increases. But the relationship with surface heat flux  
726 is less pronounced for MLD than for SST because the MLD is also influenced  
727 by the stratification in the profile below the mixed layer, and also is more  
728 directly affected by wind driven mixing.

### 729 5.6. Longer time scales

730 In May and June, at periods between approximately 4 and 20 days, the  
731 cumulative total surface heat flux is in anti-phase with the observed MLD  
732 (figure 11), and approximately in phase with the observed SST (figure 10),  
733 i.e., surface heat flux increases, MLD shoals, SST increases. These can be  
734 seen as the main warming events in SST, clearly related to large changes in  
735 MLD in the spring (figure 5). All the models exhibit similar behaviour. This  
736 timescale is typical for the passage of weather regimes. Wind stress is also a  
737 factor in these events both through the effect of wind driven mixing on the  
738 MLD and through the effect of wind speed on the latent and sensible heat  
739 fluxes.

740 There is clear evidence of a coherent relationship between wind stress and  
741 MLD for all models and the observations from late March onwards (figure 12)  
742 at periods between 4 and 60 days. MLD and wind stress are approximately  
743 in phase (i.e., wind stress increases, mixed layer deepens), though with the  
744 MLD lagging the wind stress by around an eighth of a cycle. This highlights  
745 the significance of local wind events in the spring, which can temporarily  
746 deepen the mixed layer. During the year observed, such spring deepening  
747 events reached as much as 100 m which is likely to be significant for spring  
748 bloom dynamics (Erickson and Thompson, 2018). No such relationship with  
749 local wind events is seen earlier in the year, despite the generally stronger  
750 wind stress in autumn and winter than spring and summer. We hypothesize  
751 that the deepening of the mixed layer seen in the autumn is so strongly  
752 driven by the annual cycle in surface heat flux that the additional effect of  
753 the winds at this time of year is less significant.

754 There is also some evidence of a coherent relationship between SST in the  
755 models and wind stress (figure 13), from March onwards. This is a lagged  
756 anti-phase relationship, i.e., as wind stress decreases, SST increases but with

757 a lag of approximately an eighth of a cycle or less. This is due to the shoaling  
 758 of the mixed layer as wind stress decreases: a shallower mixed layer will mean  
 759 the effect of the surface heat flux will be concentrated in a thinner band of  
 760 water, and in the spring the surface heat flux will tend to warm the ocean.  
 761 Hence SST increases as the wind stress decreases. The relationship between  
 762 wind stress and observed SST is much more tenuous than with the model  
 763 SSTs, due to the processes in the real ocean and atmosphere not present in

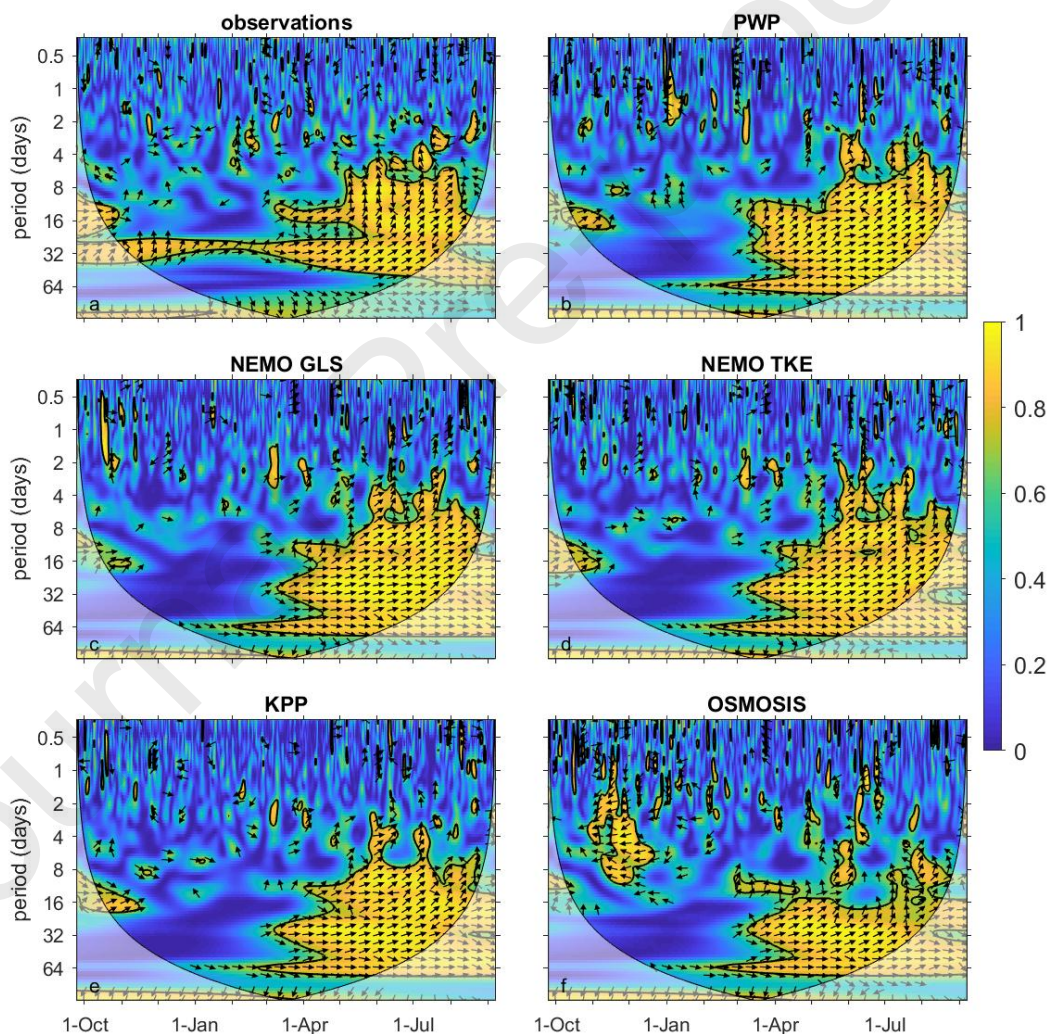


Figure 12: Wavelet coherence for MLD and wind stress. Otherwise as in figure 10.



764 the models nor in the reanalysis surface forcing.

## 765 6. Conclusions

766 Five mixed layer models driven by ERA-Interim surface forcing have been  
 767 compared with a year of observations in the North Atlantic. All the mod-

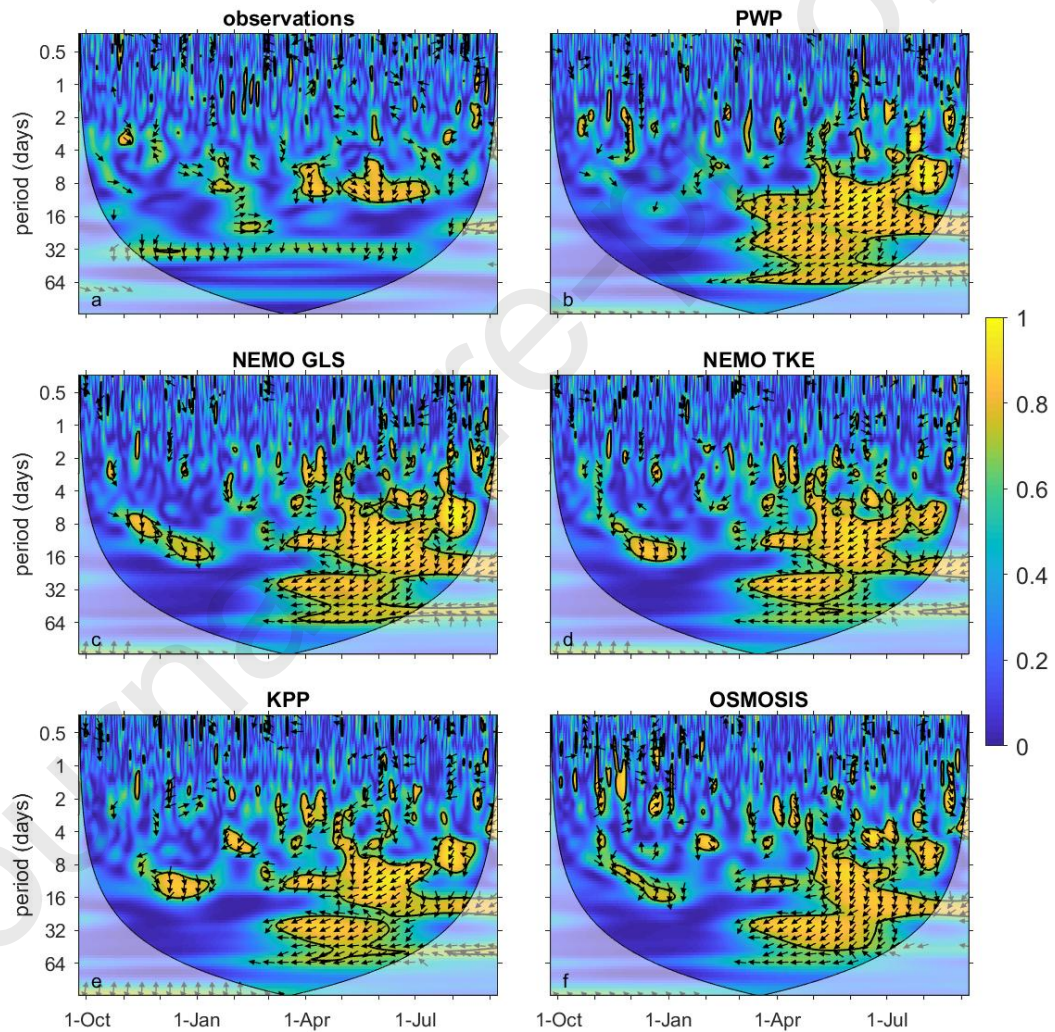


Figure 13: Wavelet coherence for SST and wind stress. Otherwise as in figure 10.

768 els reproduce SST fairly well in terms of the annual cycle, except that the  
769 KPP model has summer SSTs which are approximately  $3^{\circ}\text{C}$  warmer than  
770 the observations. Short timescale variability in SST is not predicted well by  
771 the models, likely due to the many sources of variability in SST not present  
772 in a 1-D model. The models do not reproduce the observed MLS well, but  
773 this is not unexpected as advection is expected to play a role in MLS in  
774 this region, and because precipitation biases are not uncommon in reanalysis  
775 surface forcing data. The biases are large enough to produce a non-trivial  
776 density bias. In particular, the slightly cooler temperatures and higher salin-  
777 ities in the winter in all models would lead to the formation of ENACW of  
778 greater density than that in the real ocean, which could have related effects  
779 on ocean circulation. However, this does not seem to affect the subsequent  
780 spring restratification and evolution of the MLD and SST.

781 Both the wind stress and surface heat flux are involved in driving periods  
782 of temporary deepening and shoaling of the MLD through the spring, though  
783 the effects of wind stress are felt throughout spring and summer whereas the  
784 surface heat flux is only a factor in May and June. Wind stress is not related  
785 to MLD during the autumn despite the high wind stresses in autumn. We  
786 hypothesize that the deepening of the MLD in autumn is so strongly driven  
787 by the annual cycle in surface heat flux that the winds are less significant in  
788 the autumn.

789 The surface heat flux also drives a diurnal cycle in MLD and SST from  
790 March onwards, though this effect is much clearer in the models than in the  
791 observations. We believe this is because the models and reanalysis forcing  
792 data do not include a number of processes which complicate the observed  
793 SST and MLD, so the diurnal cycle is less apparent in the observations.

794 We are not able to say that one model is 'better' than the others, they  
795 all have strengths and weaknesses. PWP has the lowest bias in spring MLD,  
796 second lowest in summer MLD, but it has the largest biases in autumn and  
797 winter MLD. Similarly it has the lowest biases in winter and spring SST, but  
798 fairly large SST biases in autumn and summer. KPP's IMLD has by far the  
799 smallest deep bias in winter, but KPP also has by far the largest bias in SST.  
800 TKE has the smallest annual mean bias in MLD but the second largest bias  
801 in spring SST. GLS has the second smallest annual mean bias and smallest  
802 rms difference in SST, but the largest bias in annual mean MLS and largest  
803 rms difference for MLS. OSMOSIS has the smallest bias in annual mean  
804 MLS, but the second largest bias in annual mean MLD and SST.

805 It is noticeable that all models had low biases in MLD in spring and sum-

mer despite the MLS and MLD biases in the preceding winter. This suggests that initializing these models using a relatively low resolution profile (e.g., from an Argo float) in late winter when stratification is low may give a quite reasonable spring stratification, which could be useful in regions where higher resolution profiles capable of resolving a steep pycnocline are not available. The variability in winter time MLD, which may be of significance for nutrient fluxes and winter bloom dynamics, is reproduced much better by model IMLDs than model MLDs.

Given the lack of differences between them, any of these models would give similar results when used for modelling in seasonal areas similar to the OSMOSIS site, i.e., at mid latitudes away from topography.

## 7. Acknowledgments

We thank the scientists, technicians, officers and crew of *RRS Discovery* cruise D381, *RV Celtic Explorer* cruise CE13001 and *RRS James Cook* cruises JC085, JC087 and JC090, especially those who went out of their way to accommodate our glider deployments. We thank the many people involved in ship-based and glider data collection, processing, sampling and calibration. The observational data used in this study were the result of five research cruises and a full year of glider piloting and involved many contributions not represented in the author list. This work was supported by NERC grants NE/I019905/1, NE/I020083/1 and NSF award OCE 1155676. GMD and KJH were supported by the European Research Council under the European Union's Horizon 2020 research and innovation programme (grant agreement n° 741120). We thank Louise Biddle and Nicholas Klingaman for useful discussions on running PWP and KPP respectively.

The observational data are held at the British Oceanographic Data Centre and can be accessed at <https://doi.org/10/cqc6>. The ERA-Interim data were obtained from the European Centre for Medium-Range Weather Forecasts (downloaded from <http://www.ecmwf.int/en/research/climatereanalysis/era-interim> in April 2016). North Atlantic Oscillation index data were provided by the Climate Analysis Section, National Centre for Atmospheric Research, Boulder, Colorado, downloaded from <http://climatedataguide.ucar.edu/guidance/hurrellnorth-atlantic-oscillation-nao-index-pc-based> in October 2014.

839 **8. References**

- 840 Abdella, K., McFarlane, N., 1997. A new second-order turbulence closure  
841 scheme for the Planetary boundary layer. *J. Atmos. Sci.* 54, 1850–1867.  
842 doi:10.1175/1520-0469(1997)054<1850:ANSOTC>2.0.CO;2.
- 843 Acreman, D.M., Jeffery, C.D., 2007. The use of Argo for valida-  
844 tion and tuning of mixed layer models. *Ocean Modell.* 19, 53–69.  
845 doi:10.1016/j.ocemod.2007.06.005.
- 846 Archer, D., Emerson, S., Powell, T., Wong, C.S., 1993. Numerical hindcasting  
847 of sea-surface pCO<sub>2</sub> at Weathership Station Papa. *Prog. Oceanogr.* 32,  
848 319–351. doi:10.1016/0079-6611(93)90019-A.
- 849 Belcher, S.E., Grant, A.L.M., Hanley, K.E., Fox-Kemper, B., Van Roekel, L.,  
850 Sullivan, P.P., Large, W.G., Brown, A., Hines, A., Calvert, D., Rutgersson,  
851 A., Pettersson, H., Bidlot, J.R., Janssen, P.A.E.M., Polton, J.A., 2012. A  
852 global perspective on Langmuir turbulence in the ocean surface boundary  
853 layer. *Geophys. Res. Lett.* 39, L18605. doi:10.1029/2012GL052932.
- 854 Biddle, L.C., Heywood, K.J., Kaiser, J., Jenkins, A., 2017. Glacial meltwa-  
855 ter identification in the Amundsen Sea. *J. Phys. Oceanogr.* 47, 933–954.  
856 doi:10.1175/JPO-D-16-0221.1.
- 857 Binetti, U., Kaiser, J., Damerell, G.M., Rumyantseva, A., Martin, A.P.,  
858 Henson, S., Heywood, K.J., this issue. Net community oxygen production  
859 derived from Seaglider deployments at the Porcupine Abyssal Plain site  
860 (PAP; northeast Atlantic) in 2012-13. *Prog. Oceanogr.* .
- 861 Blanke, B., Delecluse, P., 1993. Variability of the tropical Atlantic  
862 Ocean simulated by a general-circulation model with two different mixed-  
863 layer physics. *J. Phys. Oceanogr.* 23, 1363–1388. doi:10.1175/1520-  
864 0485(1993)023<1363:VOTTAO>2.0.CO;2.
- 865 de Boyer Montegut, C., Madec, G., Fischer, A.S., Lazar, A., Iudicone, D.,  
866 2004. Mixed layer depth over the global ocean: An examination of pro-  
867 file data and a profile-based climatology. *J. Geophys. Res.* 109, C12003.  
868 doi:10.1029/2004JC002378.
- 869 Burchard, H., Bolding, K., 2001. Comparative analysis of four  
870 second-moment turbulence closure models for the oceanic mixed



- 871 layer. *J. Phys. Oceanogr.* 31, 1943–1968. doi:10.1175/1520-  
872 0485(2001)031;1943:CAOFSM;2.0.CO;2.
- 873 Burchard, H., Craig, P.D., Gemrich, J.R., van Haren, H., Mathieu, P.P.,  
874 Meier, H.M., Smith, W.A.M.N., Prandke, H., Rippeth, T.P., Skyllingstad,  
875 E.D., et al., 2008. Observational and numerical modeling methods for  
876 quantifying coastal ocean turbulence and mixing. *Prog. Oceanogr.* 76,  
877 399–442.
- 878 Chen, D., Rothstein, L.M., Busalacchi, A.J., 1994. A hybrid vertical mixing  
879 scheme and its application to tropical ocean models. *J. Phys. Oceanogr.* 24,  
880 2156–2179. doi:10.1175/1520-0485(1994)024<2156:AHVMSA>2.0.CO;2.
- 881 Damerell, G.M., Heywood, K.J., Thompson, A.F., Binetti, U., Kaiser, J.,  
882 2016. The vertical structure of upper ocean variability at the Porcu-  
883 pine Abyssal Plain during 2012–2013. *J. Geophys. Res.* 121, 3075–3089.  
884 doi:10.1002/2015JC011423.
- 885 Dee, D.P., Uppala, S.M., Simmons, A.J., Berrisford, P., Poli, P., Kobayashi,  
886 S., Andrae, U., Balmaseda, M.A., Balsamo, G., Bauer, P., Bechtold, P.,  
887 Beljaars, A.C.M., van de Berg, L., Bidlot, J., Bormann, N., Delsol, C., Dra-  
888 gani, R., Fuentes, M., Geer, A.J., Haimberger, L., Healy, S.B., Hersbach,  
889 H., Holm, E.V., Isaksen, L., Kallberg, P., Koehler, M., Matricardi, M., Mc-  
890 Nally, A.P., Monge-Sanz, B.M., Morcrette, J..J., Park, B..K., Peubey, C.,  
891 de Rosnay, P., Tavolato, C., Thepaut, J..N., Vitart, F., 2011. The ERA-  
892 Interim reanalysis: configuration and performance of the data assimilation  
893 system. *Quart. J. Roy. Meteor. Soc.* 137, 553–597. doi:10.1002/qj.828.
- 894 Erickson, Z.K., Thompson, A.F., 2018. The seasonality of physically-driven  
895 export in the northeast Atlantic Ocean. *Global Biogeochem. Cycles* 32,  
896 1144–1162. doi:10.1029/2018GB005927.
- 897 Farahat, A., Abuelgasim, A., 2019. Role of atmospheric nutrient pollu-  
898 tion in stimulating phytoplankton growth in small area and shallow depth  
899 water bodies: Arabian Gulf and the sea of Oman. *Atmos. Environ.* ,  
900 117045doi:10.1016/j.atmosenv.2019.117045.
- 901 Flato, G., Marotzke, J., Abiodun, B., Braconnot, P., Chou, S., Collins,  
902 W., Cox, P., Driouech, F., Emori, S., Eyring, V., Forest, C., Gleck-  
903 ler, P., Guilyardi, E., Jakob, C., Kattsov, V., Reason, C., Rum-

- 904 mukainen, M., 2013. Evaluation of Climate Models. pp. 741–866.  
905 doi:10.1017/CBO9781107415324.
- 906 Frants, M., Gille, S.T., Hatta, M., Hiscock, W.T., Kahru, M., Measures,  
907 C.I., Mitchell, B.G., Zhou, M., 2013. Analysis of horizontal and vertical  
908 processes contributing to natural iron supply in the mixed layer in southern  
909 Drake Passage. *Deep-Sea Res* 90, 68–76. doi:10.1016/j.dsr2.2012.06.001.
- 910 Gaspar, P., Grégoris, Y., Lefevre, J.M., 1990. A simple eddy kinetic energy  
911 model for simulations of the oceanic vertical mixing: Tests at station Papa  
912 and long-term upper ocean study site. *J. Geophys. Res.* 95, 16179–16193.
- 913 Giglio, D., Gille, S.T., Subramanian, A.C., Nguyen, S., 2017. The role of  
914 wind gusts in upper ocean diurnal variability. *J. Geophys. Res.* 122, 7751–  
915 7764. doi:10.1002/2017JC012794.
- 916 Grant, A.L.M., Belcher, S.E., 2009. Characteristics of Langmuir turbu-  
917 lence in the ocean mixed layer. *J. Phys. Oceanogr.* 39, 1871–1887.  
918 doi:10.1175/2009JPO4119.1.
- 919 Grinsted, A., Moore, J.C., Jevrejeva, S., 2004. Application of the cross  
920 wavelet transform and wavelet coherence to geophysical time series. *Non-  
921 linear Processes Geophys.* 11, 561–566. doi:10.5194/npg-11-561-2004.
- 922 Harcourt, R.R., 2013. A second-moment closure model of Langmuir turbu-  
923 lence. *J. Phys. Oceanogr.* 43, 673–697. doi:10.1175/JPO-D-12-0105.1.
- 924 Harcourt, R.R., 2015. An improved second-moment closure model of Lang-  
925 muir turbulence. *J. Phys. Oceanogr.* 45, 84–103. doi:10.1175/JPO-D-14-  
926 0046.1.
- 927 Hartman, S.E., Jiang, Z.P., Turk, D., Lampitt, R.S., Frigstad, H., Ostle, C.,  
928 Schuster, U., 2015. Biogeochemical variations at the Porcupine Abyssal  
929 Plain sustained Observatory in the northeast Atlantic Ocean, from weekly  
930 to inter-annual timescales. *Biogeosciences* 12, 845–853. doi:10.5194/bg-12-  
931 845-2015.
- 932 Hartman, S.E., Lampitt, R.S., Larkin, K.E., Pagnani, M., Campbell, J.,  
933 Gkritzalis, T., Jiang, Z.P., Pebody, C.A., Ruhl, H.A., Gooday, A.J.,  
934 Bett, B.J., Billett, D.S.M., Provost, P., McLachlan, R., Turton, J.D.,  
935 Lankester, S., 2012. The Porcupine Abyssal Plain fixed-point sustained

- 936 observatory (PAP-SO): variations and trends from the Northeast Atlantic  
937 fixed-point time-series. *ICES Journal of Marine Science* 69, 776–783.  
938 doi:10.1093/icesjms/fss077.
- 939 Hartman, S.E., Larkin, K.E., Lampitt, R.S., Lankhorst, M., Hydes, D.J.,  
940 2010. Seasonal and inter-annual biogeochemical variations in the Porcu-  
941 pine Abyssal Plain 2003-2005 associated with winter mixing and surface  
942 circulation. *Deep-Sea Res.* 57, 1303–1312. doi:10.1016/j.dsr2.2010.01.007.
- 943 Harvey, J., 1982. Theta-S relationships and water masses in the eastern North  
944 Atlantic. *Deep-Sea Res.* 29, 1021–1033. doi:10.1016/0198-0149(82)90025-5.
- 945 Henson, S., Lampitt, R., Johns, D., 2012. Variability in phytoplankton  
946 community structure in response to the North Atlantic Oscillation and  
947 implications for organic carbon flux. *Limnol. Oceanogr.* 57, 1591–1601.  
948 doi:10.4319/lo.2012.57.6.1591.
- 949 Hirons, L.C., Klingaman, N.P., Woolnough, S.J., 2015. MetUM-GOML1: a  
950 near-globally coupled atmosphere ocean-mixed-layer model. *Geosci. Model*  
951 *Dev.* 8, 363–379. doi:10.5194/gmd-8-363-2015.
- 952 Hirons, L.C., Klingaman, N.P., Woolnough, S.J., 2018. The impact of air-  
953 sea interactions on the representation of tropical precipitation extremes.  
954 *J. Adv. Model. Earth Syst.* 10, 550–559. doi:10.1002/2017MS001252.
- 955 Holtslag, A.A.M., Moeng, C.H., 1991. Eddy diffusivity and countergradient  
956 transport in the convective atmospheric boundary layer. *J. Atmos. Sci.* 48,  
957 1690–1698. doi:10.1175/1520-0469(1991)048<1690:EDACTI>2.0.CO;2.
- 958 Kantha, L.H., Clayson, C.A., 1994. An improved mixed-layer model  
959 for geophysical applications. *J. Geophys. Res.* 99, 25235–25266.  
960 doi:10.1029/94JC02257.
- 961 Kim, J.W., 1976. A generalized bulk model of the oceanic  
962 mixed layer. *J. Phys. Oceanogr.* 6, 686–695. doi:10.1175/1520-  
963 0485(1976)006<0686:AGBMOT>2.0.CO;2.
- 964 Kraus, E.B., Turner, J.S., 1967. A one-dimensional model of the seasonal  
965 thermocline II. The general theory and its consequences. *Tellus* 19, 98–106.  
966 doi:10.1111/j.2153-3490.1967.tb01462.x.

- 967 Lampitt, R.S., Billett, D.S.M., Martin, A.P., 2010a. The sustained ob-  
968 servatory over the Porcupine Abyssal Plain (PAP): Insights from time  
969 series observations and process studies. *Deep-Sea Res.* 57, 1267–1271.  
970 doi:10.1016/j.dsr2.2010.01.003.
- 971 Lampitt, R.S., Salter, I., de Cuevas, B.A., Hartman, S., Larkin, K.E., Pe-  
972 body, C.A., 2010b. Long-term variability of downward particle flux in the  
973 deep northeast Atlantic: causes and trends. *Deep-Sea Res.* 57, 1346–1361.  
974 doi:10.1016/j.dsr2.2010.01.011.
- 975 Large, W.G., McWilliams, J.C., Doney, S.C., 1994. Oceanic vertical mixing  
976 - a review and a model with a nonlocal boundary-layer parameterization.  
977 *Rev. Geophys.* 32, 363–403. doi:10.1029/94RG01872.
- 978 Large, W.G., Yeager, S.G., 2009. The global climatology of an inter-  
979 annually varying air-sea flux data set. *Climate Dyn.* 33, 341–364.  
980 doi:10.1007/s00382-008-0441-3.
- 981 Lazarevich, P., Rossby, T., McNeil, C., 2004. Oxygen variability in the near-  
982 surface waters of the northern North Atlantic: observations and a model.  
983 *J. Mar. Res.* 62, 663–683. doi:10.1357/0022240042387547.
- 984 Lazarevich, P., Stoermer, S., 2001. A Matlab ver-  
985 sion of the Price, Weller, Pinkel model. URL:  
986 <http://www.po.gso.uri.edu/rafos/research/pwp/>.
- 987 Lee, J.C.K., Klingaman, N.P., 2018. The effect of the quasi-biennial oscil-  
988 lation on the Madden-Julian oscillation in the Met Office Unified Model  
989 global ocean mixed layer configuration. *Atmos. Sci. Lett.* 19, UNSP e816.  
990 doi:10.1002/asl.816.
- 991 Li, Q., Fox-Kemper, B., 2017. Assessing the effects of Langmuir turbulence  
992 on the entrainment buoyancy flux in the ocean surface boundary layer. *J.*  
993 *Phys. Oceanogr.* 47, 2863–2886. doi:10.1175/JPO-D-17-0085.1.
- 994 Li, Q., Webb, A., Fox-Kemper, B., Craig, A., Danabasoglu, G., Large,  
995 W.G., Vertenstein, M., 2016. Langmuir mixing effects on global cli-  
996 mate: WAVEWATCH III in CESM. *Ocean Modell.* 103, 145–160.  
997 doi:10.1016/j.ocemod.2015.07.020.

- 998 Madec, G., 2008. NEMO ocean engine: Note du Ple de modlisation, Institut  
999 Pierre-Simon Laplace (IPSL), France, No 27, ISSN No 1288-1619.
- 1000 Martin, A.P., Lucas, M.I., Painter, S.C., Pidcock, R., Prandke, H.,  
1001 Prandke, H., Stinchcombe, M.C., 2010. The supply of nutrients due  
1002 to vertical turbulent mixing: A study at the Porcupine Abyssal Plain  
1003 study site in the northeast Atlantic. *Deep-Sea Res.* 57, 1293–1302.  
1004 doi:10.1016/j.dsr2.2010.01.006.
- 1005 Martz, T.R., Johnson, K.S., Riser, S.C., 2008. Ocean metabolism observed  
1006 with oxygen sensors on profiling floats in the South Pacific. *Limnol.*  
1007 *Oceanogr.* 53, 2094–2111. doi:10.4319/lo.2008.53.5\_part.2.2094.
- 1008 McWilliams, J.C., Sullivan, P.P., Moeng, C.H., 1997. Langmuir turbulence  
1009 in the ocean. *J. Fluid Mech.* 334, 1–30.
- 1010 Mellor, G.L., Yamada, T., 1982. Development of a turbulence closure model  
1011 for geophysical fluid problems. *Rev. Geophys.* 20, 851–875.
- 1012 Paulson, C.A., Simpson, J.J., 1977. Irradiance measurements in the  
1013 upper ocean. *J. Phys. Oceanogr.* 7, 952–956. doi:10.1175/1520-  
1014 0485(1977)007<0952:IMITUO>2.0.CO;2.
- 1015 Pearson, B.C., Grant, A.L.M., Polton, J.A., Belcher, S.E., 2015. Langmuir  
1016 turbulence and surface heating in the ocean surface boundary layer. *J.*  
1017 *Phys. Oceanogr.* 45, 2897–2911. doi:10.1175/JPO-D-15-0018.1.
- 1018 Pollard, R.T., Griffiths, M.J., Cunningham, S.A., Read, J.F., Perez, F.F.,  
1019 Rios, A.F., 1996. Vivaldi 1991-A study of the formation, circulation and  
1020 ventilation of Eastern North Atlantic Central Water. *Prog Oceanogr* 37.  
1021 doi:10.1016/S0079-6611(96)00008-0.
- 1022 Pollard, R.T., Pu, S., 1985. Structure and circulation of the Upper At-  
1023 lantic Ocean northeast of the Azores. *Prog Oceanogr* 14, 443–462.  
1024 doi:10.1016/0079-6611(85)90022-9.
- 1025 Pookkandy, B., Dommenges, D., Klingaman, N., Wales, S., Chung, C.,  
1026 Frauen, C., Wolff, H., 2016. The role of local atmospheric forcing on the  
1027 modulation of the ocean mixed layer depth in reanalyses and a coupled sin-  
1028 gle column ocean model. *Climate Dyn.* 47, 2991–3010. doi:10.1007/s00382-  
1029 016-3009-7.

- 1030 Price, J.F., Mooers, C.N.K., Vanleer, J.C., 1978. Observation and simulation  
1031 of storm-induced mixed-layer deepening. *J. Phys. Oceanogr.* 8, 582–599.  
1032 doi:10.1175/1520-0485(1978)008<0582:OASOSI>2.0.CO;2.
- 1033 Price, J.F., Weller, R.A., Pinkel, R., 1986. Diurnal cycling - observations and  
1034 models of the upper ocean response to diurnal heating, cooling, and wind  
1035 mixing. *J. Geophys. Res.* 91, 8411–8427. doi:10.1029/JC091iC07p08411.
- 1036 Refray, G., Bourdalle-Badie, R., Calone, C., 2015. Modelling turbulent  
1037 vertical mixing sensitivity using a 1-D version of NEMO. *Geosci. Model*  
1038 *Dev.* 8, 69–86.
- 1039 Rodgers, K.B., Aumont, O., Fletcher, S.M., Plancherel, Y., Bopp, L.,  
1040 Montégut, C.D.B., Iudicone, D., Keeling, R., Madec, G., Wanninkhof, R.,  
1041 2014. Strong sensitivity of Southern Ocean carbon uptake and nutrient  
1042 cycling to wind stirring. *Biogeosciences* 11, 4077–4098.
- 1043 Rodi, W., 1987. Examples of calculation methods for flow and mixing in  
1044 stratified fluids. *J. Geophys. Res.* 92, 5305–5328.
- 1045 Rumyantseva, A., S., H., Martin, A.P., Thompson, A.F., Damerell, G.M.,  
1046 Kaiser, J., Heywood, K.J., this issue. Phytoplankton spring bloom initia-  
1047 tion: The impact of atmospheric forcing and light in the temperate North  
1048 Atlantic Ocean. *Prog. Oceanogr.* .
- 1049 Sharples, J., Ross, O.N., Scott, B.E., Greenstreet, S.P.R., Fraser, H., 2006.  
1050 Inter-annual variability in the timing of stratification and the spring  
1051 bloom in the North-western North Sea. *Cont. Shelf Res.* 26, 733–751.  
1052 doi:10.1016/j.csr.2006.01.011.
- 1053 Sheehan, P.M.F., Berx, B., Gallego, A., Hall, R.A., Heywood, K.J., Hughes,  
1054 S.L., Queste, B.Y., 2018. Shelf sea tidal currents and mixing fronts  
1055 determined from ocean glider observations. *Ocean Sci.* 14, 225–236.  
1056 doi:10.5194/os-14-225-2018.
- 1057 Simonot, J.Y., Le Treut, H., 1986. A climatological field of mean op-  
1058 tical properties of the World Ocean. *J. Geophys. Res.* 91, 6642–6646.  
1059 doi:10.1029/JC091iC05p06642.

- 1060 Steinhoff, T., Friedrich, T., Hartman, S.E., Oschlies, A., Wallace, D.W.R.,  
1061 Kortzinger, A., 2010. Estimating mixed layer nitrate in the North Atlantic  
1062 Ocean. *Biogeosciences* 7, 795–807. doi:10.5194/bg-7-795-2010.
- 1063 Stips, A., 2011. Fitting measured irradiance of Jerlov water types to double  
1064 exponential functions using R.
- 1065 Taylor (ed.), P., 2000. Final report of the joint WCRP/SCOR Working Group  
1066 on air-sea fluxes: intercomparison and validation of ocean-atmosphere en-  
1067 ergy flux fields, WCRP-112, WMO/TD-No.1036, World Climate Research  
1068 Programme, 303 pp.
- 1069 Thompson, A.F., Lazar, A., Buckingham, C., Naveira Garabato, A.C.,  
1070 Damerell, G.M., Heywood, K.J., 2016. Open-ocean submesoscale motions:  
1071 A full seasonal cycle of mixed layer instabilities from gliders. *J. Phys.*  
1072 *Oceanogr.* 46, 1285–1307. doi:10.1175/JPO-D-15-0170.1.
- 1073 Torrence, C., Compo, G.P., 1998. A practical guide to wavelet analysis. *Bull.*  
1074 *Amer. Meteor. Soc.* 79, 61–78.
- 1075 Torrence, C., Webster, P., 1999. Interdecadal changes in the ENSO-monsoon  
1076 system. *J. Climate* 12, 2679–2690.
- 1077 Umlauf, L., Burchard, H., 2003. A generic length-scale equation for geophys-  
1078 ical turbulence models. *J. Mar. Res.* 61, 235–265.
- 1079 Van Roekel, L., Adcroft, A.J., Danabasoglu, G., Griffies, S.M., Kauffman,  
1080 B., Large, W., Levy, M., Reichl, B.G., Ringler, T., Schmidt, M., 2018.  
1081 The KPP boundary layer scheme for the ocean: revisiting its formulation  
1082 and benchmarking one-dimensional simulations relative to LES. *J. Adv.*  
1083 *Model. Earth Syst.* 10, 2647–2685. doi:10.1029/2018MS001336.
- 1084 Viglione, G.A., Thompson, A.F., Flexas, M.M., Sprintall, J., Swart, S., 2018.  
1085 Abrupt transitions in submesoscale structure in southern Drake Passage:  
1086 glider observations and model results. *J. Phys. Oceanogr.* 48, 2011–2027.  
1087 doi:10.1175/JPO-D-17-0192.1.
- 1088 Wilcox, D.C., 1988. Reassessment of the scale-determining equation for ad-  
1089 vanced turbulence models. *AIAA journal* 26, 1299–1310.



1090 Yang, B., Emerson, S.R., Bushinsky, S.M., 2017. Annual net community  
1091 production in the subtropical Pacific Ocean from in situ oxygen mea-  
1092 surements on profiling floats. *Global Biogeochem. Cycles* 31, 728–744.  
1093 doi:10.1002/2016GB005545.

## Highlights

Unique, year-long, high resolution glider dataset compared with 5 mixed layer models.

Model winter mixed layers are too deep, with average biases between 160 and 228 m.

After spring restratification, biases in MLD are small and unrelated to winter biases.

Model biases in mixed layer salinity produce non-trivial density biases, but this does not affect the subsequent spring and summer MLD and SST.

**Declaration of interests**

The authors declare that they have no known competing financial interests or personal relationships that could have appeared to influence the work reported in this paper.

The authors declare the following financial interests/personal relationships which may be considered as potential competing interests:

Journal Pre-proofs